10. V. Southgate, A. Senju, G. Csibra, *Psychol. Sci.* **18**, 587–592 (2007).
11. D. C. Marticorena, A. M. Ruiz, C. Mukerji, A. Goddu, L. R. Santos, *Dev. Sci.* **14**, 1406–1416 (2011).
12. A. Martin, L. R. Santos, *Cognition* **130**, 300–308 (2014).
13. F. Kano, J. Call, *Psychol. Sci.* **25**, 1691–1698 (2014).
14. F. Kano, S. Hirata, *Curr. Biol.* **25**, 2513–2517 (2015).
15. Materials and methods are available as supplementary materials on *Science* Online.
16. J. Perner, T. Ruffman, *Science* **308**, 214–216 (2005).
17. C. Heyes, *Dev. Sci.* **17**, 647–659 (2014).
18. R. Baillargeon, R. M. Scott, Z. He, *Trends Cogn. Sci.* **14**, 110–118 (2010).
19. A. Senju, V. Southgate, C. Snape, M. Leonard, G. Csibra, *Psychol. Sci.* **22**, 878–880 (2011).
20. K. Karg, M. Schmelz, J. Call, M. Tomasello, *Anim. Behav.* **105**, 211–221 (2015).

ACKNOWLEDGMENTS

We thank the staff at the Wolfgang Kohler Primate Research Center and Kumamoto Sanctuary for assistance. Financial support was provided by the NSF Graduate Research Fellowship Program (grant DGE-1106401 to C.K.), the Ministry of Education, Culture, Sports, Science and Technology of Japan (grant K-CONNEX to F.K.), the Japan Society for the Promotion of Science (grants KAKENHI 26885040 and 16K21108 to F.K. and grants KAKENHI 26245069 and 24000001 to S.H.), and the European Research Council (Synergy grant 609819 to J.C.). Data are available in the main text and supplementary materials.

SUPPLEMENTARY MATERIALS

www.sciencemag.org/content/354/6308/110/suppl/DC1
Materials and Methods
Supplementary Text
Figs. S1 to S5
Tables S1 to S5
Movies S1 and S2

27 April 2016; accepted 26 August 2016
10.1126/science.aaf8110

STRUCTURAL BIOLOGY

The methanogenic CO_2 reducing-and-fixing enzyme is bifunctional and contains 46 [4Fe-4S] clusters

Tristan Wagner,[1] Ulrich Ermler,[2] Seigo Shima[1,3]*

Biological methane formation starts with a challenging adenosine triphosphate (ATP)–independent carbon dioxide (CO_2) fixation process. We explored this enzymatic process by solving the x-ray crystal structure of formyl-methanofuran dehydrogenase, determined here as Fwd(ABCDFG)$_2$ and Fwd(ABCDFG)$_4$ complexes, from *Methanothermobacter wolfeii*. The latter 800-kilodalton apparatus consists of four peripheral catalytic sections and an electron-supplying core with 46 electronically coupled [4Fe-4S] clusters. Catalysis is separately performed by subunits FwdBD (FwdB and FwdD), which are related to tungsten-containing formate dehydrogenase, and subunit FwdA, a binuclear metal center carrying amidohydrolase. CO_2 is first reduced to formate in FwdBD, which then diffuses through a 43-angstrom-long tunnel to FwdA, where it condenses with methanofuran to formyl-methanofuran. The arrangement of [4Fe-4S] clusters functions as an electron relay but potentially also couples the four tungstopterin active sites over 206 angstroms.

Methanogenic archaea produce ~1 billion tons of methane per year and thus play an important ecological role in the global carbon cycle (*1*). Biological methane is produced mainly from acetate and CO_2-H_2 (*1*). For methanogenesis from CO_2, the metabolic pathway starts with the reduction of CO_2 to form formyl-methanofuran (formyl-MFR) (E_0' = −530 mV, where E_0' is the standard redox potential at pH 7) (*2*), using reduced ferredoxin (E' = ~−500 mV, where E' is a physiological redox potential at pH 7) (*1*) as the electron donor (Fig. 1A). The reaction is catalyzed by formyl-MFR dehydrogenase. There are two isoenzymes in most methanogens, a tungsten iron-sulfur protein (Fwd) and a molybdenum iron-sulfur protein (Fmd) (*3*–*9*).

Formyl-MFR dehydrogenase uses CO_2 rather than bicarbonate as a substrate (*10*, *11*). CO_2 spontaneously reacts with MFR to form carboxy-MFR at a rate that is compatible with carboxy-MFR being an intermediate in CO_2 reduction to formyl-MFR (*10*, *11*). Therefore, it was assumed that carboxy-MFR is reduced to formyl-MFR in a subsequent step at the tungsten or molybdenum active site of formyl-MFR dehydrogenases. This reaction sequence is in line with all other CO_2-fixing enzymatic processes, except for that of acetogenesis, where CO_2 is first reduced to formate and then conjugated with N-10 of tetrahydrofolate using adenosine triphosphate (ATP) (*12*).

To elucidate the catalytic mechanism of this sequence, we purified and crystallized the tungstopterin-containing formyl-MFR dehydrogenase (FwdABCDFG) complex from the thermophilic methanogenic archaeon *Methanothermobacter wolfeii* (fig. S1) under strict anoxic conditions in four crystal forms (table S1) (*13*). The x-ray analysis of individual subunit structures and, subsequently, of the whole protein complex is primarily based on orthorhombic and triclinic crystals diffracting to 1.9 and 2.6 Å resolution, in which the enzyme is present as a dimer of the FwdABCDFG heterohexamer [12-subunit oligomer (12-mer)] (Fig. 1B and fig. S2A) and a tetramer of the heterohexamer (24-mer) (fig. S2B), respectively. Notably, FwdF and FwdG were absent in gel electrophoresis but are integral components of the enzyme complex.

Subunit FwdA (63 kDa) is structurally classified as a member of the amidohydrolase superfamily, which includes urease, phosphotriesterase, dihydroorotase, and dihydropyrimidinases (fig. S3) (*7*–*9*). These enzymes are characterized by a binuclear metal center positioned inside a deep solvent-accessible cavity at the entry of an $(\alpha/\beta)_8$ TIM barrel. The metal center is predicted to be composed of two zinc atoms that are analogous to the most structurally related enzyme, dihydroorotase (*14*). FwdA also contains zinc ligands, N6-carboxylysine, and a catalytically crucial aspartate, all of which are strictly conserved in the amidohydrolase superfamily (Fig. 2D and figs. S3A and S4). The x-ray structure of the triclinic 24-mer crystals soaked with MFR revealed the bulky C1 carrier in the cavity between the dinuclear metal center and the bulk solvent (Fig. 2D and fig. S4).

Subunit FwdB (48 kDa) harbors the tungstopterin active site and a [4Fe-4S] cluster. This subunit is structurally related to domains I, II, and III of molybdenum- and tungsten-containing formate dehydrogenase (*7*–*9*); FwdD (14 kDa) is structurally related to domain IV (*7*–*9*). A solution nuclear magnetic resonance structure of FwdD from *Archaeoglobus fulgidus* has been reported (Protein Data Bank ID: 2KI8). The redox-active tungsten of FwdBD (FwdB and FwdD) is coordinated by four dithiolene thiolates of two tungstopterin guanine dinucleotide molecules (Fig. 2, A to C), by the thiolate of Cys^{118}, and by an inorganic sulfido ligand (fig. S5). The residues involved in the [4Fe-4S] cluster, pterin-binding, tungsten-ligation, and active sites are essentially conserved between FwdBD and the molybdenum- or tungsten-containing formate dehydrogenases (*15*–*18*). FwdC (29 kDa) is a subunit with low sequence similarity to the C-terminal domain of glutamate synthase (*19*), flanking the tunnel that channels ammonia between the two active sites.

FwdF (39 kDa) is a polyferredoxin composed of four similar ferredoxin domains (*7*–*9*) that are arranged in a T-shaped conformation (Fig. 1C and figs. S6 and S7). The fusion of the ferredoxin domains, each carrying two [4Fe-4S] clusters, does not occur consecutively; the third ferredoxin domain (amino acids 143 to 221) is inserted into the second ferredoxin domain (amino acids 106 to 137 and 228 to 257) (fig. S7A). FwdG (8.6 kDa) adopts a classical ferredoxin fold that hosts two [4Fe-4S] clusters.

The 12-mer has an electron-supplying core (two FwdFG subunits) and two flanking catalytic sections, each formed by FwdA and FwdBD.

[1]Max Planck Institute for Terrestrial Microbiology, Karl-von-Frisch-Straße 10, 35043 Marburg, Germany. [2]Max Planck Institute of Biophysics, Max-von-Laue-Straße 3, 60438 Frankfurt am Main, Germany. [3]Precursory Research for Embryonic Science and Technology (PRESTO), Japan Science and Technology Agency (JST), 332-0012 Saitama, Japan.
*Corresponding author. Email: shima@mpi-marburg.mpg.de

Likewise, the 24-mer core (four FwdFG subunits) is flanked by four catalytic sections. The FwdA and FwdBD subunits harbor one active site each, such that both reactions proceed spatially separated from each other (Fig. 2, A and B). In contrast to previous proposals, the structural data strongly suggest that in the first step, CO_2 is reduced to formate (E_0' = −430 mV) by ferredoxin (E' = ~−500 mV) at the tungstopterin active site in FwdBD; the protons required for the reaction could be supplied by a hydrophilic cavity filled with plenty of water molecules (figs. S8 and S9). This revision is in accordance with the high structural similarity between FwdBD and tungsten- or molybdenum-containing formate dehydrogenases and the direct connection with the adjacent electron-supplying system (see below) (Fig. 2C). The molybdenum-containing formyl-MFR dehydrogenase isoenzymes (Fmd) from *M. wolfeii* and *Methanosarcina barkeri* are known to exhibit weak formate oxidation activity (*3*, *4*), which supports our proposal. The deeply buried redox-active tungsten center is only connected with the bulk solvent via a narrow hydrophobic tunnel that is 40 Å long (fig. S10). Therefore, the active site is accessible to CO_2 but not to formate, the formate transition state analog azide (*20*), and the bulky MFR.

In a subsequent step, the produced formate is covalently bound to the amino group of MFR to generate formyl-MFR at the second active site localized in FwdA. This reaction was deduced from the high similarity of the active sites between FwdA and other enzymes of the amidohydrolase superfamily (*14*). In particular, the production of formate from formyl-MFR catalyzed by an FwdABC homolog (FhcABC from methylotrophic bacteria that is devoid of the pterin cofactor) underlines our conclusion (*21*). Moreover, the determined structure of the FwdA-MFR complex revealed a mechanistically relevant active-site geometry (Fig. 2D and fig. S4); the catalytically active amino group of MFR directly interacts with the binuclear metal site and Asp^{385} (Fig. 2D and fig. S4). On the basis of this finding and detailed information of a related amidohydrolase catalyzing the analogous formation of dihydroorotate from carbamoyl aspartate (*14*), we postulated a plausible catalytic mechanism for the reaction between formate and MFR to generate formyl-MFR (fig. S11).

The proposed two-step scenario of CO_2 reduction and fixation is further corroborated by an internal hydrophilic tunnel (43 Å long) between the active sites of FwdBD and FwdA, which is ideally suited for the transport of formate and formic acid [pK_a = 3.75 (K_a, acid dissociation constant)] (Fig. 2B and fig. S12). The tunnel consists of a wide solvent-filled cavity with a narrow passage in front of each active site (Figs. 2B and 3). Arg^{288} of FwdB and Lys^{64} of FwdA are positioned at these bottlenecks and might control gate opening and closing, with the aim of arresting formate until MFR binding. Supplemented formate is not used as a substrate by FwdABCDFG from *M. wolfeii* (*3*, *4*), which is consistent with a completely tight tunnel between the active sites inside the FwdABCDFG protein complex. Release or uptake of formate into or from the solution is then impossible. The weak formate oxidation activity of the aforementioned molybdenum-containing isoenzymes (*3*, *4*) suggests a leaky tunnel. Tunneling of intermediates has been reported for several bifunctional enzymes, such as glutamate synthase (fig. S13) and the carbon monoxide dehydrogenase–acetyl-CoA synthase complex (*22*, *23*), to allow for the migration of small molecules in a facilitated one-directional diffusion process, thus optimizing catalysis (*24*).

Considering that under standard conditions at pH 7.0 the formation of formyl-MFR from formate and MFR is an endergonic reaction (Gibbs free energy change $\Delta G^{\circ\prime}$ = +12 to 19 kJ/mol) (*2*), energy coupling with the exergonic reduction of CO_2 to formate with reduced ferredoxin might be accomplished by pumping formate into the encapsulated tunnel to increase its local concentration. The only sequentially related CO_2 reduction-and-fixation

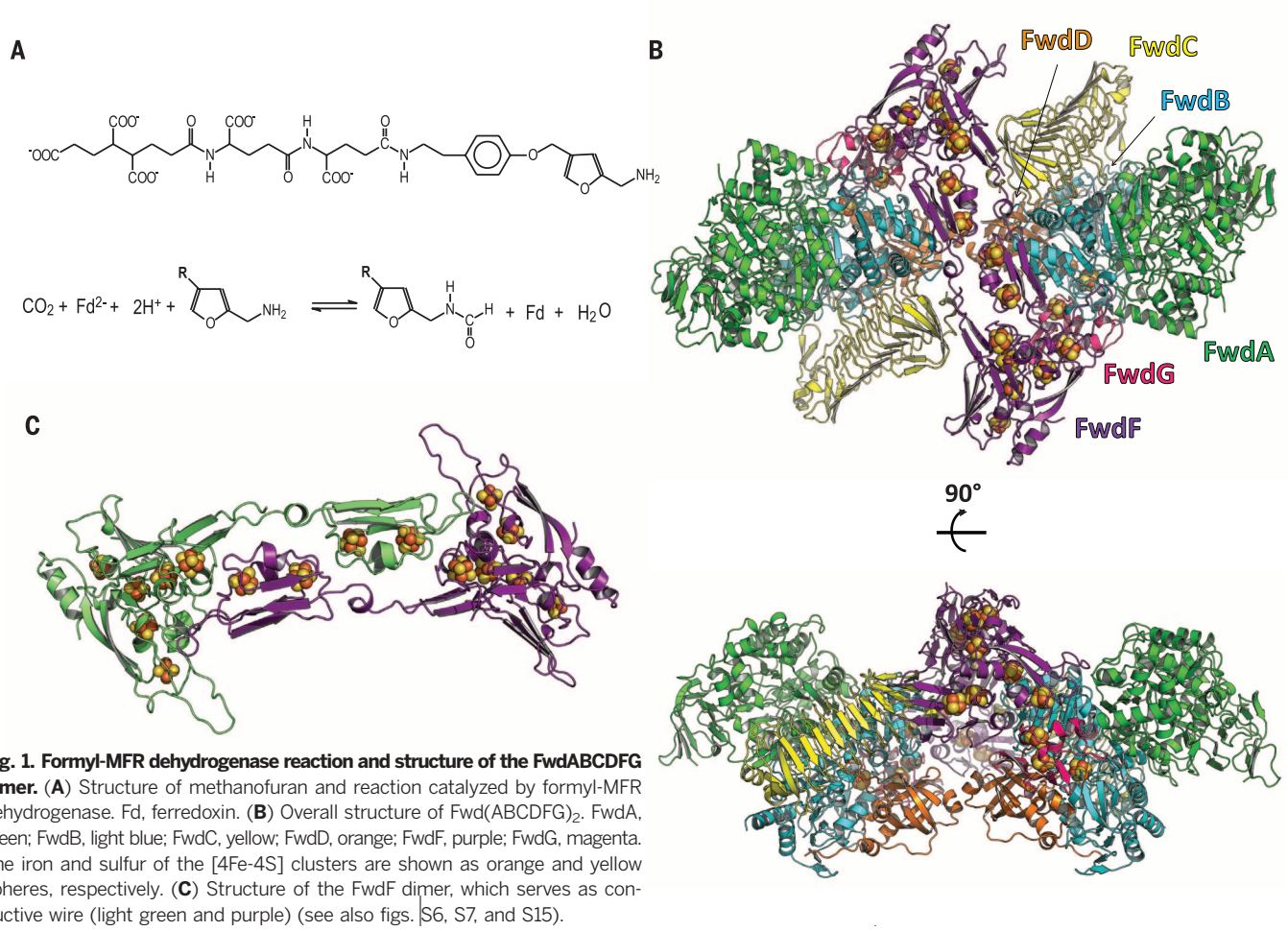

Fig. 1. Formyl-MFR dehydrogenase reaction and structure of the FwdABCDFG dimer. (**A**) Structure of methanofuran and reaction catalyzed by formyl-MFR dehydrogenase. Fd, ferredoxin. (**B**) Overall structure of Fwd(ABCDFG)$_2$. FwdA, green; FwdB, light blue; FwdC, yellow; FwdD, orange; FwdF, purple; FwdG, magenta. The iron and sulfur of the [4Fe-4S] clusters are shown as orange and yellow spheres, respectively. (**C**) Structure of the FwdF dimer, which serves as conductive wire (light green and purple) (see also figs. S6, S7, and S15).

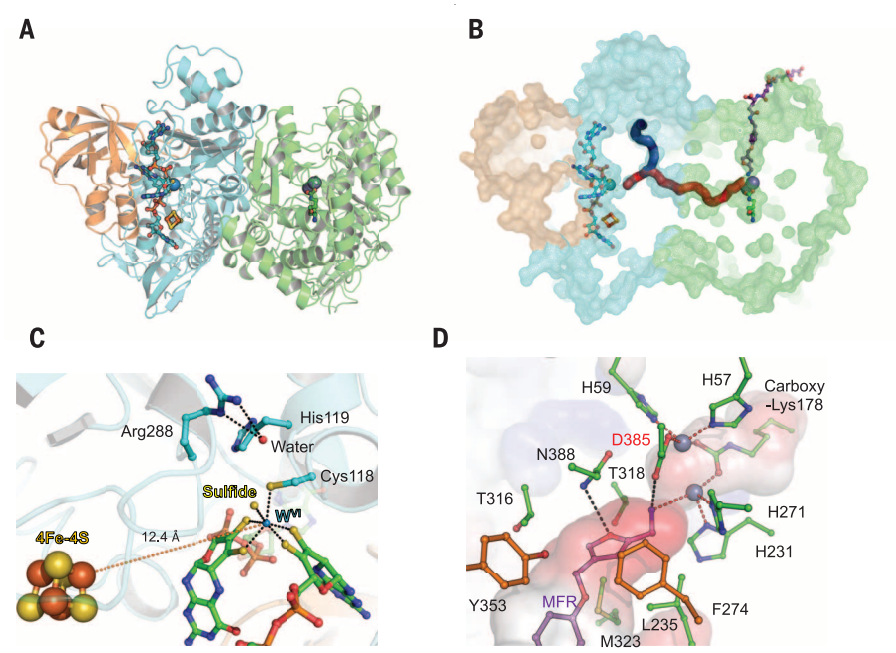

Fig. 2. Structures of the FwdABD subcomplex. (**A**) Catalytic subunits. The amidohydrolase FwdA (green) and the formate dehydrogenase FwdBD (light blue, orange) are shown. Tungstopterin (carbon in blue), the [4Fe-4S] cluster (orange and yellow), and the carboxylysine (carbon in green) at the binuclear zinc center are depicted as ball-and-stick models. (**B**) Surface model of FwdABD with cofactors and MFR (purple). The proposed formate tunnel (in red, solid surface) connects the active sites of FwdB and FwdA, and the narrow CO_2 tunnel (dark blue, solid surface) exclusively allows CO_2 to reach the tungsten center from the bulk solvent. (**C**) Active site of FwdB. The tungsten (light blue) of tungstopterin (green) is coordinated by six sulfurs (yellow) in a distorted octahedral arrangement. The space between Cys^{118}, the inorganic sulfur tungsten ligand, His^{119}, and Arg^{228} is occupied by solvent but appears to be well suited for CO_2 binding (*17*). (**D**) Active site of FwdA bound to MFR. The two zinc ions are coordinated to four histidines and an N6-carboxylysine protruding from the cavity bottom. One zinc ion is ligated to the catalytically essential Asp^{385}. Aromatic (orange) and hydrophobic side chains flank the *p*-(β-aminoethyl)phenoxymethyl group. The 2-aminomethylfuran moiety is anchored to the polypeptide by two hydrogen bond donors and one π-stacking interaction with Phe^{274}. Coordination of the binuclear center and the hydrogen bonds of the MFR to the protein are indicated by red and black dashed lines, respectively. The electrostatic surface of the protein is shown in the gradient from red (acidic) to blue (basic). H, His; N, Asn; D, Asp; T, Thr; Y, Tyr; F, Phe; L, Leu; M, Met.

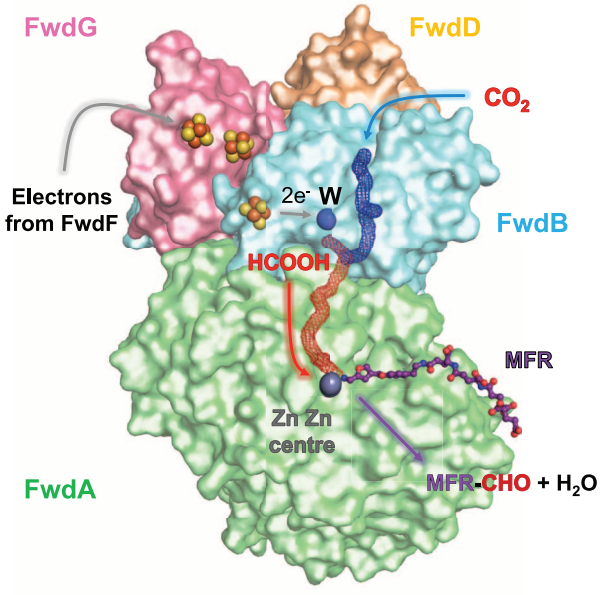

Fig. 3. Proposed mechanism of CO_2 reduction to formyl-MFR catalyzed by the FwdABCDFG complex. Electrons (e^-) are funneled through the [4Fe-4S] cluster chain to the tungsten center. CO_2 enters the catalytic chamber through a hydrophobic tunnel (blue mesh) of FwdBD and is reduced to formate; W^{IV} is oxidized to W^{VI}. Formic acid (or formate) diffuses via a hydrophilic tunnel (red mesh) to the active site of FwdA, where it is condensed with MFR at the binuclear zinc center (gray sphere).

process found in acetogenesis is catalyzed by two separate enzymes, formate dehydrogenase and formyl-tetrahydrofolate synthetase, the latter of which requires ATP for formate activation.

In the 24-mer, two 12-mers are associated in an hourglass-like arrangement (Fig. 4), thereby furnished with an additional [4Fe-4S] cluster per each 12-mer that covalently links the two FwdF subunits (fig. S6). The two extra [4Fe-4S] clusters in the 24-mer are 7.7 Å apart from each other and 10.3 Å away from the next [4Fe-4S] cluster (figs. S2B and S14), which allows interdodecameric electron shuttling (Fig. 4 and fig. S15). The cysteine ligands of the two additional [4Fe-4S] clusters originating from both FwdF subunits are fully conserved in methanogens without cytochromes, except for those belonging to Methanomicrobiales. The residues of the surrounding loop, which are involved in interdodecameric interactions, are also conserved to a great extent (fig. S14). In addition, the 24-mer was observed in another crystal form [$P3_221$ (fig. S2B and table S1], which grew in a different crystallization solution (see supplementary materials). Finally, formyl-MFR dehydrogenase appears to make a huge complex with heterodisulfide reductase and other catabolic enzymes (*25*, *26*), which may stabilize the 24-mer FwdABCDFG structure. Therefore, the 24-meric supercomplex is assumed to be a physiologically active state and not a crystallographic artifact.

The 46 [4Fe-4S] clusters in the 24-mer are arranged in a stringlike distribution (Fig. 4). The edge-to-edge distances of 8.6 to 12.4 Å are characteristic of electrically connected redox centers (fig. S15) (*27*, *28*). Because polar and charged residues are known to affect the redox potential of iron-sulfur clusters (*29*), their similar surroundings concerning structure and electrostatics suggest that electrons are conducted almost isopotentially, without obvious thermodynamic barriers. The formed electron wire extends over distances of 188 Å between the redox-active tungsten centers of the 12-mer. The 24-mer uses the interdodecamer bridge between the two wires of the 12-mers to extend over 206 Å between active sites. The outer cluster of the two [4Fe-4S] clusters in the branched peripheral arm of the T-shaped FwdF subunits might serve as the entry point for electrons (Fig. 4) from where the electrons flow to the tungsten center via a chain of optimally spaced [4Fe-4S] clusters. Association between the formyl-MFR dehydrogenase complex and the electron-bifurcating [NiFe]-hydrogenase–heterodisulfide reductase complex (MvhABD-HdrABC) (*25*) implicates a long, direct electron transfer route from the site of electron bifurcation (HdrA) to the site of CO_2 reduction (FwdBD), perhaps via the FwdF entry point.

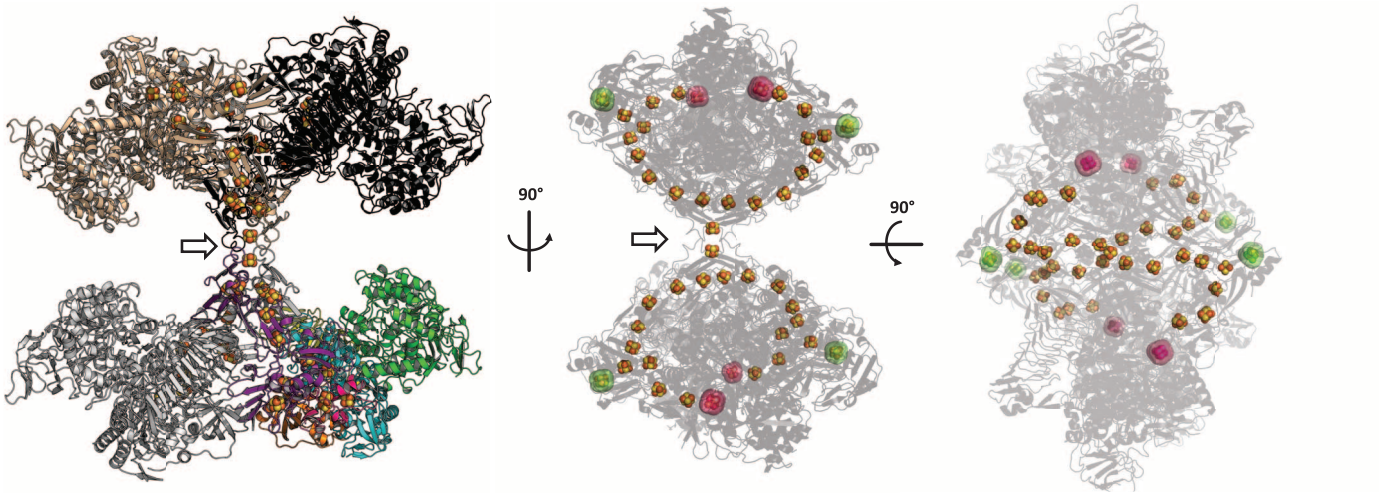

Fig. 4. Structure of the tetrameric FwdABCDFG supercomplex. (**Left**) Hourglass-shaped arrangement of the two Fwd(ABCDFG)$_2$ complexes (24-mer). The four heterohexamers are shown in black, gray, beige, and multicolor (the color code is the same as in Fig. 1B). The iron and sulfur of the [4Fe-4S] clusters are shown as orange and yellow spheres, respectively. (**Middle** and **Right**) Transparent side views. The four green [4Fe-4S] clusters mark the postulated entry point for the electrons; the four pink [4Fe-4S] clusters are the clusters next to tungsten. The two 12-mers interact via the two FwdF dimers, each with an extra [4Fe-4S] cluster (arrows).

It is unlikely that such a sophisticated apparatus of 46 electronically coupled [4Fe-4S] clusters evolved simply for supplying low-potential electrons for CO_2 reduction. Therefore, we assume an additional function regarding the 24-mer Fwd complex and, more broadly, methanogenic energy metabolism. For example, the four tungstopterin redox centers may couple each other over 206 Å and may also couple to the preceding enzymatic process reducing the [4Fe-4S] clusters for synchronizing the redox reactions. Alternatively, these clusters may function to store reducing equivalents in a manner similar to multicytochromes (*30*) and multiheme enzymes (*31*). A low-potential electron pool would allow for reaction flexibility with temporally varying amounts of CO_2.

REFERENCES AND NOTES

1. R. K. Thauer, A. K. Kaster, H. Seedorf, W. Buckel, R. Hedderich, *Nat. Rev. Microbiol.* **6**, 579–591 (2008).
2. P. A. Bertram, R. K. Thauer, *Eur. J. Biochem.* **226**, 811–818 (1994).
3. P. A. Bertram *et al.*, *Eur. J. Biochem.* **220**, 477–484 (1994).
4. R. A. Schmitz, S. P. J. Albracht, R. K. Thauer, *Eur. J. Biochem.* **209**, 1013–1018 (1992).
5. R. A. Schmitz, S. P. J. Albracht, R. K. Thauer, *FEBS Lett.* **309**, 78–81 (1992).
6. R. A. Schmitz, M. Richter, D. Linder, R. K. Thauer, *Eur. J. Biochem.* **207**, 559–565 (1992).
7. A. Hochheimer, R. A. Schmitz, R. K. Thauer, R. Hedderich, *Eur. J. Biochem.* **234**, 910–920 (1995).
8. A. Hochheimer, R. Hedderich, R. K. Thauer, *Arch. Microbiol.* **170**, 389–393 (1998).
9. A. Hochheimer, D. Linder, R. K. Thauer, R. Hedderich, *Eur. J. Biochem.* **242**, 156–162 (1996).
10. S. Bartoschek, J. A. Vorholt, R. K. Thauer, B. H. Geierstanger, C. Griesinger, *Eur. J. Biochem.* **267**, 3130–3138 (2000).
11. J. A. Vorholt, R. K. Thauer, *Eur. J. Biochem.* **248**, 919–924 (1997).
12. L. R. Celeste *et al.*, *Protein Sci.* **21**, 219–228 (2012).
13. Materials and methods are available as supplementary materials on *Science* Online.
14. J. B. Thoden, G. N. Phillips Jr., T. M. Neal, F. M. Raushel, H. M. Holden, *Biochemistry* **40**, 6989–6997 (2001).
15. J. C. Boyington, V. N. Gladyshev, S. V. Khangulov, T. C. Stadtman, P. D. Sun, *Science* **275**, 1305–1308 (1997).
16. H. Raaijmakers *et al.*, *Structure* **10**, 1261–1272 (2002).
17. L. B. Maia, J. J. G. Moura, I. Moura, *J. Biol. Inorg. Chem.* **20**, 287–309 (2015).
18. M. Jormakka, S. Törnroth, B. Byrne, S. Iwata, *Science* **295**, 1863–1868 (2002).
19. C. Binda *et al.*, *Structure* **8**, 1299–1308 (2000).
20. J. S. Blanchard, W. W. Cleland, *Biochemistry* **19**, 3543–3550 (1980).
21. B. K. Pomper, O. Saurel, A. Milon, J. A. Vorholt, *FEBS Lett.* **523**, 133–137 (2002).
22. H. Dobbek, V. Svetlitchnyi, L. Gremer, R. Huber, O. Meyer, *Science* **293**, 1281–1285 (2001).
23. T. I. Doukov, T. M. Iverson, J. Seravalli, S. W. Ragsdale, C. L. Drennan, *Science* **298**, 567–572 (2002).
24. X. Huang, H. M. Holden, F. M. Raushel, *Annu. Rev. Biochem.* **70**, 149–180 (2001).
25. K. C. Costa *et al.*, *Proc. Natl. Acad. Sci. U.S.A.* **107**, 11050–11055 (2010).
26. K. C. Costa, T. J. Lie, Q. Xia, J. A. Leigh, *J. Bacteriol.* **195**, 5160–5165 (2013).
27. A. Volbeda *et al.*, *Nature* **373**, 580–587 (1995).
28. J. W. Peters, W. N. Lanzilotta, B. J. Lemon, L. C. Seefeldt, *Science* **282**, 1853–1858 (1998).
29. S. Santabarbara, P. Heathcote, M. C. W. Evans, *Biochim. Biophys. Acta* **1708**, 283–310 (2005).
30. A. Esteve-Núñez, J. Sosnik, P. Visconti, D. R. Lovley, *Environ. Microbiol.* **10**, 497–505 (2008).
31. K. D. Bewley, K. E. Ellis, M. A. Firer-Sherwood, S. J. Elliott, *Biochim. Biophys. Acta* **1827**, 938–948 (2013).

ACKNOWLEDGMENTS

We thank R. Thauer for discussions and helpful suggestions, H. Michel for support, J. Koch for laboratory maintenance, the staff of the Swiss Light Source (Villigen, Switzerland) for help with data collection, and A. Poehlein for genome sequencing at the Institute of Microbiology and Genetics of the Georg August University Göttingen. This work was supported by grants from the Max Planck Society (to R. Thauer, S.S., and U.E.) and the PRESTO program from the JST (to S.S.). Structure factors and models have been deposited in the Protein Data Bank under identification numbers 5T5I (12-mer, $P2_12_12_1$), 5T61 (24-mer bound MFR, $P1$), and 5T5M (12-mer, $P3_221$).

SUPPLEMENTARY MATERIALS

www.sciencemag.org/content/354/6308/114/suppl/DC1
Materials and Methods
Figs. S1 to S15
Table S1
References (*32*–*43*)

18 May 2016; accepted 2 September 2016
10.1126/science.aaf9284

The methanogenic CO_2 reducing-and-fixing enzyme is bifunctional and contains 46 [4Fe-4S] clusters

Tristan Wagner, Ulrich Ermler and Seigo Shima (October 6, 2016)

Science **354** (6308), 114-117. [doi: 10.1126/science.aaf9284]

Editor's Summary

The long and winding road to methane

The process by which archaea make methane involves a series of reactions and enzymes. First, CO_2 and methanofuran (MFR) are reduced to formyl-MFR by an as yet unresolved mechanism. Wagner *et al.* solved the x-ray crystal structure of a tungsten-containing formyl-MFR dehydrogenase complex. Two active sites in the complex are separated by a 43-Å tunnel, which is responsible for transferring the formate made after CO_2 reduction. The complex also contains a chain of 46 iron-sulfur clusters. Although the exact function of this chain is unclear, it may electronically couple the four tungsten redox centers.

Science, this issue p. 114

Science (print ISSN 0036-8075; online ISSN 1095-9203) is published weekly, except the last week in December, by the American Association for the Advancement of Science, 1200 New York Avenue NW, Washington, DC 20005.

www.sciencemag.org/content/354/6308/114/suppl/DC1

Supplementary Materials for

The methanogenic CO_2 reducing-and-fixing enzyme is bifunctional and contains 46 [4Fe-4S] clusters

Tristan Wagner, Ulrich Ermler, Seigo Shima*

*Corresponding author. Email: shima@mpi-marburg.mpg.de

Published 7 October 2016, *Science* **354**, 114 (2016)
DOI: 10.1126/science.aaf9284

This PDF file includes:

Materials and Methods

Methanothermobacter wolfeii culture

We structurally analyzed the formyl-methanofuran (formyl-MFR) dehydrogenase complex from *Methanothermobacter wolfeii* because this enzyme has already been well characterized biochemically (*4-6*). *M. wolfeii* (DSM 2970) was obtained from the Deutsche Sammlung von Mikroorganismen und Zellkulturen (DSMZ, Braunschweig, Germany) and was routinely grown at 65 °C in two 2 liter fermenters containing 1.5 liters of medium each. The growth medium corresponds to that used by Schmitz *et al.* (*4*), with a mixture of 0.33 mg/l $Na_2WO_4 \cdot 2H_2O$ and 0.24 mg/l $Na_2MoO_4 \cdot 2H_2O$. The cultures were gassed with 80% H_2/20% CO_2/0.01% H_2S at a rate of 0.8 liter per min and stirred at 1,000 rpm. When the culture reached an optical density of ca. 5 at 600 nm, the cells were harvested by centrifugation under anoxic conditions at 8 °C, yielding approximately 30–35 g cells (wet mass). The cell pellets were stored at −80 °C before enzyme purification.

Purification of the Fwd complex

The cell pellets were thawed at room temperature. Lysis buffer (50 mM MOPS/NaOH, pH 7.0, 10 mM $MgCl_2$ and 2 mM dithiothreitol) was added at a ratio of 2 ml per g pellet. The cells were disrupted in a French press at 7 MPa under 100% N_2 gas. The lysate was centrifuged twice at 10,000 ×*g* for 60 min, and then the supernatant was ultracentrifuged at 110,000 ×*g* for 90 min at 4 °C. The subsequent steps were performed under anoxic conditions (95% N_2/5% H_2) at 18 °C, without any freezing steps. First, the soluble fraction was passed through a DEAE Sepharose fast-flow column equilibrated with 50 mM Tricine-NaOH pH 8.0 containing 2 mM dithiothreitol (DTT) (buffer A). The protein was eluted at a flow rate of 4 ml/min with a step-wise increasing concentration of NaCl: two column volumes of 270 mM NaCl, four column volumes of 310 mM NaCl, and four column volumes of 420 mM NaCl. The 420 mM NaCl fractions containing Fwd were pooled and diluted with an equal volume of buffer A. The sample was loaded onto a Q-Sepharose fast-flow column (GE Healthcare, Freiburg) pre-equilibrated in buffer A; the column was washed with 400 mM NaCl, and the proteins were eluted at a flow rate of 3.5 ml/min with a gradient of 400–500 mM NaCl in six column volumes. Fwd typically eluted at 450–475 mM NaCl. Fractions containing Fwd were diluted with an equal volume of 25 mM sodium phosphate buffer, pH 7.6, containing 2 mM DTT (buffer B) and loaded onto a hydroxyapatite ceramic type I column (macroprep; Bio-Rad; München, Germany) equilibrated with buffer B. The column was washed with 50 mM sodium phosphate buffer, pH 7.6, and the proteins were eluted at a flow rate of 2 ml/min with a gradient of 50–150 mM sodium phosphate buffer, pH 7.6, in four column volumes. Fwd eluted at 90–140 mM sodium phosphate buffer, pH 7.6. The Fwd fractions were pooled, diluted with two volumes of 25 mM Tris/HCl, pH 7.6, containing 2.0 M $(NH_4)_2SO_4$ and 2 mM DTT, and applied to a Source 15 Phe column that had been pre-equilibrated in the same buffer. The column was washed with 0.5 M $(NH_4)_2SO_4$, and the protein was eluted at a flow rate of 1 ml/min with a gradient of 0.5–0.18 M $(NH_4)_2SO_4$ in six column volumes. Fwd eluted in two fractions: in an "early" fraction at 0.46–0.32 M $(NH_4)_2SO_4$ along with methyl-viologen-reducing hydrogenase (Mvh) (*32*) and in a "late" fraction at 0.31–0.26 M $(NH_4)_2SO_4$ alone. Both the "early" and "late" fractions were separately concentrated by passing them through a 50 kDa cut-off filter (Merck Millipore,

Darmstadt, Germany). The samples were then injected onto a 10/300 Superose 6 column (GE Healthcare) equilibrated in 25 mM Tris/HCl, pH 7.6, containing 10% glycerol and 2 mM DTT and eluted at a flow rate of 0.3 ml/min. Fwd in both samples eluted at 14 ml, and the eluted proteins from the two samples crystallized similarly. The purified preparation revealed 10–30 U/mg (*4*, *6*). One U enzyme is defined as the amount catalyzing the oxidation of 1 µmol formylmethanofuran/min under the standard assay conditions described previously (*4*). The purified enzyme was concentrated by passing the pooled fraction through a 50 kDa cut-off filter, and the final concentration was measured using the Bradford method. Each elution profile was systematically controlled by separating them on SDS-polyacrylamide gels (15%) to choose the purest fractions.

Crystallization of the Fwd complex

Three crystallization hits were obtained by initial screening using a palette of commercial kits. The best-diffracting crystals were obtained at 18 °C using the sitting drop method and a crystallization plate (CombiClover Junior Plate, Jena Bioscience, Jena, Germany); the crystallization drop contained 100 mM Tricine/NaOH, pH 8.0, 30% (v/v) pentaerythritol propoxylate 426 (5/4 PO/OH), and 400 mM KCl. The optimal concentration and volume of the protein and volume of precipitant were 30 mg/ml and 1 µl of protein and 1 µl of precipitant. Depending on the incubation time and the protein/precipitant ratio, crystal of several forms appeared under the same crystallization conditions. Controlled crystallization of only one specific crystal form was not possible, even when different temperatures, protein:precipitant ratios and additives were used. The earliest appearing crystals were brownish thin and square plates belonging to the *P*1 or $P2_1$ space group. The next crystals emerged were rod-shaped, black crystals that belong to space group $P2_12_12_1$; these diffracted best. The last crystals formed were black and thick, hexagon-shaped crystals corresponding to space group $P3_221$.

When we mixed 0.5 µl of a 15 mg protein/ml solution with 0.5 µl of 100 mM Tris/HCl, pH 9.0, containing 8% (w/v) PEG 8000, 500 mM NaCl and 30% (v/v) methylpentanediol, crystals of another form grew also in the space group $P3_221$. Unfortunately, these crystals always diffracted at a very poor resolution.

Triclinic, trigonal and high-resolution orthorhombic crystal forms were soaked for 20 min with 7 mM MFR in the crystallization solution prior to freezing. MFR only bound to the triclinic form.

Structural analysis

All crystals could be directly frozen in liquid nitrogen without cryoprotection steps. The diffraction experiments were performed at 100 K on beamline X10SA equipped with a PILATUS 6M detector at the Swiss Light Source Synchrotron (Villigen). The data were processed with iMOSFLM or XDS (*33*) and scaled with *scala* or *aimless* from the ccp4 suite (*34*). The structure of the Fwd complex was solved using the single-wavelength anomalous dispersion method by collecting a dataset of the orthorhombic crystal form at the L(III) edge of the tungsten. The tungsten atom sites were localized with SHELX C/D (*35*). The experimental electron-density map was obtained after solvent flattening using SHELX E. Automated model building was performed using ARP/wARP (*36*) and the amino acid sequence of FwdABCD. Bands corresponding to FwdF and FwdG were not detected by Coomassie-staining on the SDS-PAGE gel (fig. S1). Because the two

subunits were not expected to be part of the Fwd complex structure, FwdF and FwdG were first traced as a glycine backbone. The electron-density map was sufficiently accurate to recognize the sequence in the chain and to identify FwdF and FwdG. ARP/wARP was used to complete the model using the FwdF and FwdG sequences.

The structures of the other crystal forms were determined by molecular replacement using Molrep (ccp4 suite) (*37*) or Phaser (Phenix package) (*38*) and the coordinates of the orthorhombic crystal form as the search model. All models were manually constructed with COOT (*39*) and refined by REFMAC (*40*), except for the poorly diffracting trigonal crystal form, for which the resolution was too low for further refinement. The final refinements of orthorhombic crystal data was perfomed using BUSTER (Bricogne G., Blanc E., Brandl M., Flensburg C., Keller P., Paciorek W., Roversi P, Sharff A., Smart O.S., Vonrhein C., Womack T.O. (2016). BUSTER version 2.10.1. Cambridge, United Kingdom: Global Phasing Ltd.). The two other crystal forms, triclinic and trigonal were refined by Phenix (*38*). Restraints for non-crystallographic symmetry (NCS) were applied to all models (except for the better-diffracting trigonal crystal form, which contained only one heterohexamer in the asymmetric unit), and translation-liberation-screw-rotation (TLS) was only applied to the orthorhombic and trigonal crystal forms. The final models were validated through the MolProbity server (http://molprobity.biochem.duke.edu). Data collection, the refinement statistics of the deposited models, and the structure factors are listed in Table S1.

The figures were generated and rendered with PyMOL (Version 1.5, Schrödinger, LLC). All superposition studies were calculated using the ccp4 suite. Both tunnel cavities possibly for CO_2 and formate transfer in the protein were detected using the program CAVER 3.0 (*41*) by applying the threshold of 1.2 Å radius.

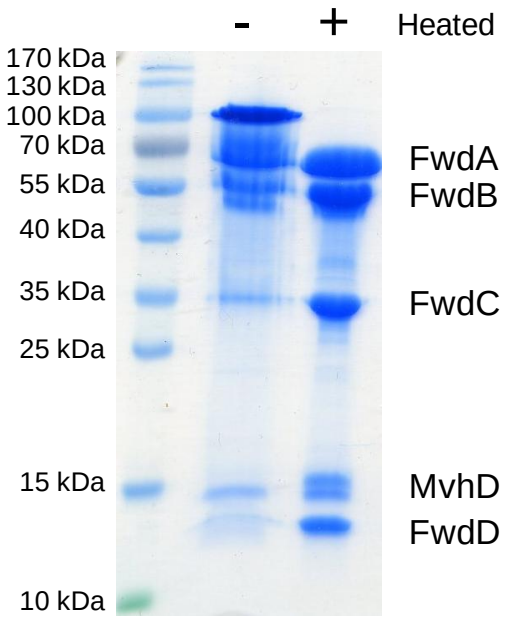

Fig. S1.

SDS-PAGE of the Fwd complex. The samples were prepared without (–) or with (+) pre-incubation at 95 °C for 5 min. The Fwd complex (6 μg) was loaded in each gel lane.

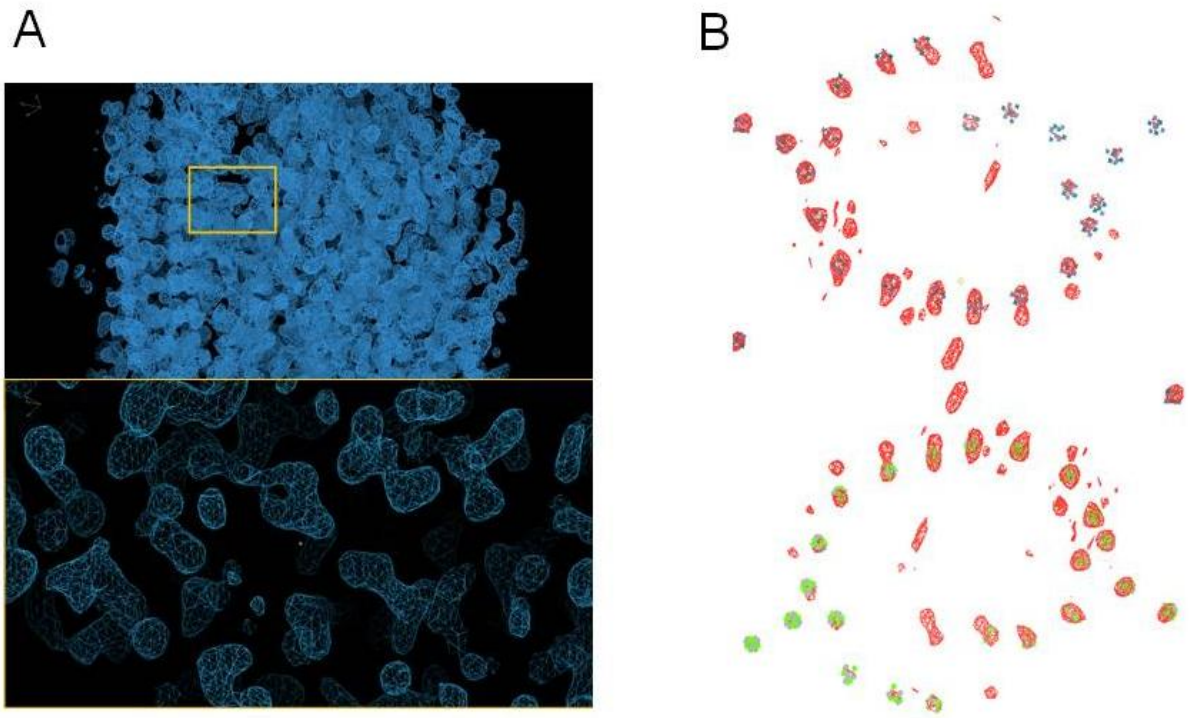

Fig. S2

Experimental electron-density map of Fwd. (**A**) Experimental electron-density map derived from data of the orthorhombic crystal form obtained after solvent flattening using SHELXE contoured at 1σ. The enlarged area (orange square) was contoured at 2σ to highlight the quality of the map. (**B**) Crystals of trigonal crystal form containing a tetramer of heterohexamers. The electron-density map of Fwd(ABCDFG)$_4$ (24-mer, in red) was obtained after phasing with PHASER and DM. The diffraction data were recorded at the tungsten LIII absorption edge. A contour level of 6.5σ for the difference electron density map was used to highlight the [4Fe-4S] cluster position. The [4Fe-4S] clusters from the 24-mer supercomplex are shown as green or blue dots.

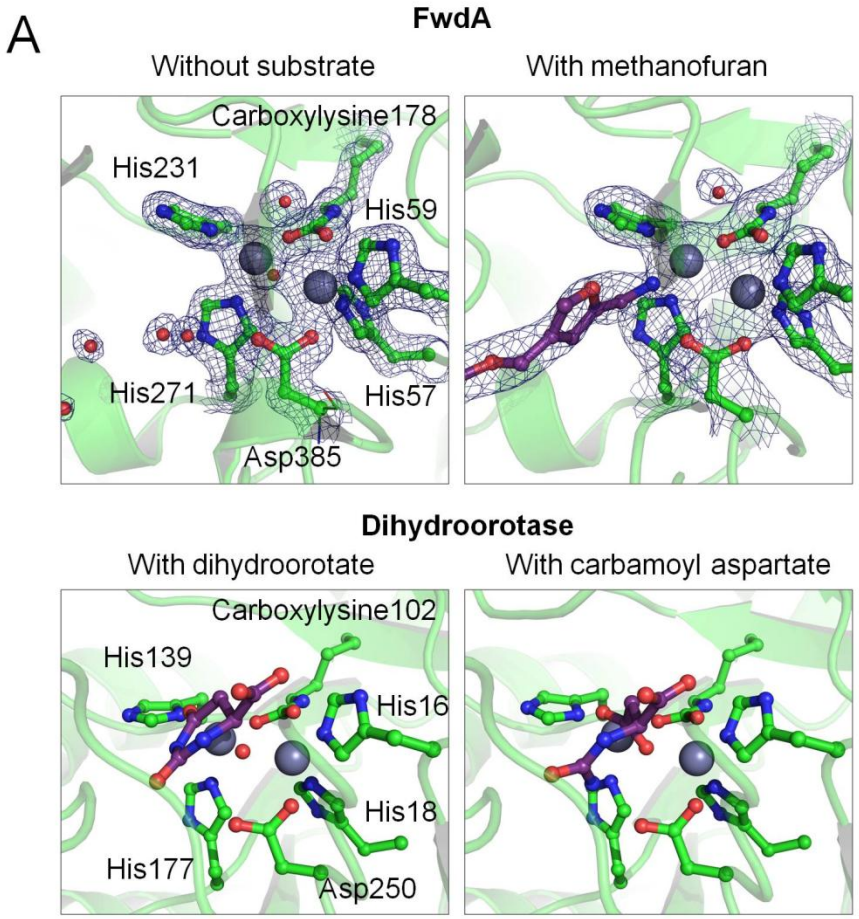
A
FwdA
Without substrate
With methanofuran
Carboxylysine178
His231
His59
His271
His57
Asp385
Dihydroorotase
With dihydroorotate
With carbamoyl aspartate
Carboxylysine102
His139
His16
His18
His177
Asp250

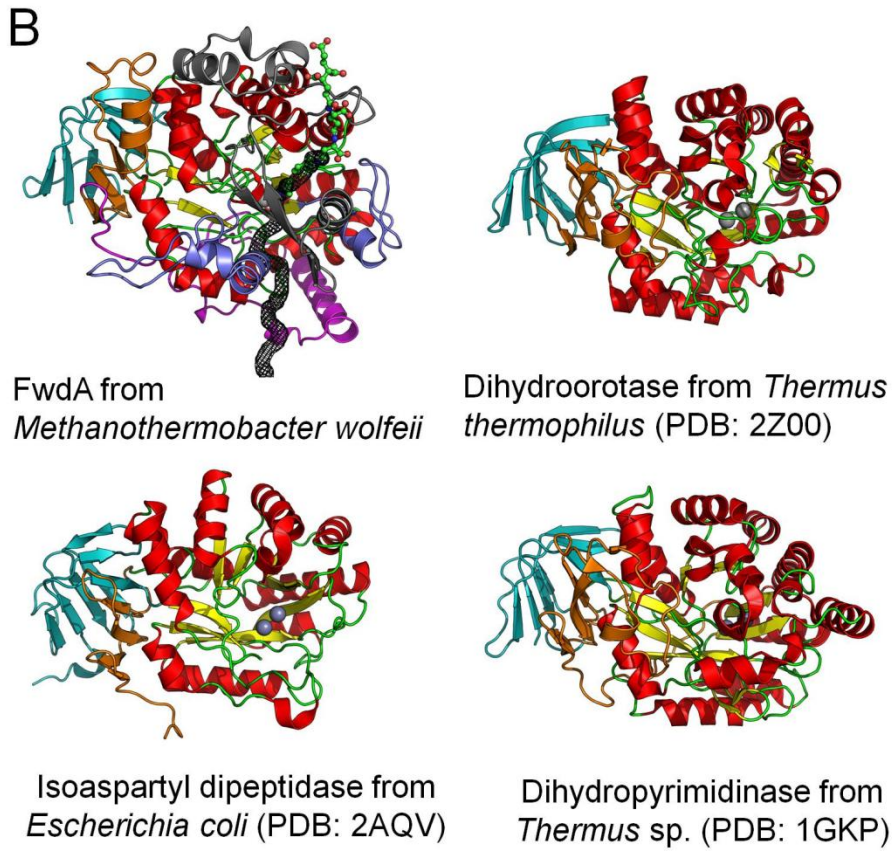
B
FwdA from
Methanothermobacter wolfeii
Dihydroorotase from Thermus
thermophilus (PDB: 2Z00)
Isoaspartyl dipeptidase from
Escherichia coli (PDB: 2AQV)
Dihydropyrimidinase from
Thermus sp. (PDB: 1GKP)

Fig. S3

Comparison of the binuclear zinc-sites and folds of FwdA and amidohydrolases. (**A**) The upper left panel represents the active site of FwdA with the two zinc ions (grey spheres) and their coordinating residues as ball-and-stick models. A network of water molecules occupying the FwdB side of the tunnel is depicted by red spheres. The upper right panel shows the structure of the FwdA–methanofuran complex. Each $2F_o$-F_c map was contoured at 1σ. In the lower panels, dihydroorotase from *Escherichia coli* with dihydroorotate and the enzyme with *N*-carbamoyl-L-aspartate (PDB: 1XGE) are presented in the same orientation. (**B**) Comparison of the folds of FwdA and class I amidohydrolases. The closest homologues of each class of amidohydrolase were compared. The common N-terminal extension is drawn in cyan, the distorted TIM barrel is drawn according to its secondary structure (helices in red, loops in green, and strands in yellow), and the C-terminal extension is shown in orange. The tunnel connecting FwdB and FwdA is shown as a black mesh, and MFR is drawn as a ball-and-stick model. Segments playing a role in MFR binding, tunnel formation and FwdBC binding are highlighted in grey, violet and magenta, respectively.

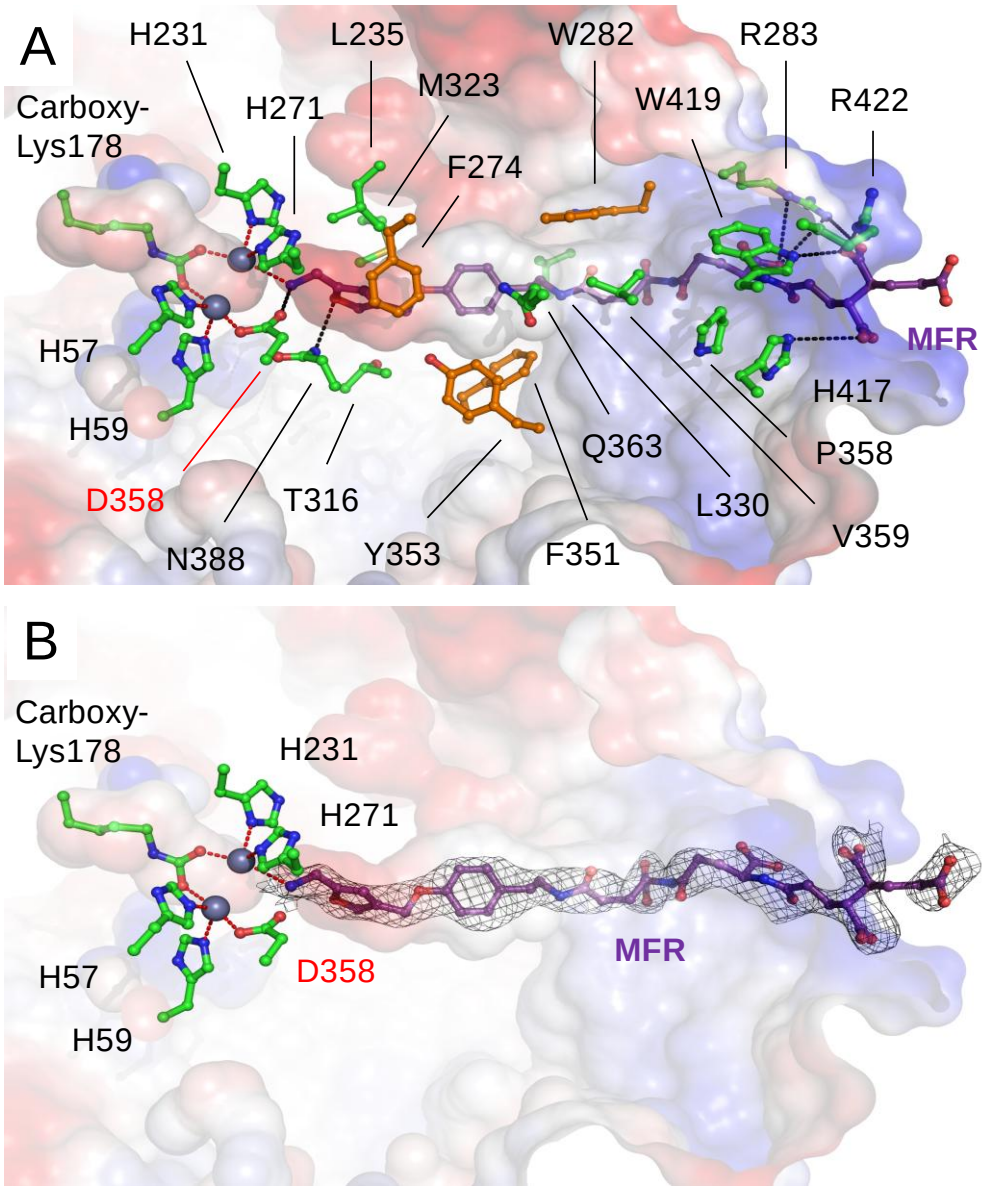

Fig. S4

The active site of FwdA bound to MFR. (**A**) The two zinc ions are coordinated to four histidines and an N6-carboxylysine protruding from the cavity bottom. One zinc ion is ligated to the catalytically essential Asp385. The 1,3,4,6-tetracarboxy-hexane moiety of MFR interacts with Arg283, His417, Arg422 and Trp419; their positive charge state is reflected in the blue surface. The two γ-linked glutamate residues hydrogen-bonded to Arg283 are positioned at the entry of the formate tunnel. Aromatic and hydrophobic side chains flank the unipolar *p*-(β-aminoethyl)phenoxymethyl group. The 2-aminomethylfuran moiety is anchored to the polypeptide by two hydrogen bond donors and one π-stacking interaction with Phe274. (**B**) The $2F_o$-F_c map around MFR is contoured at 1.0σ and shown as black mesh.

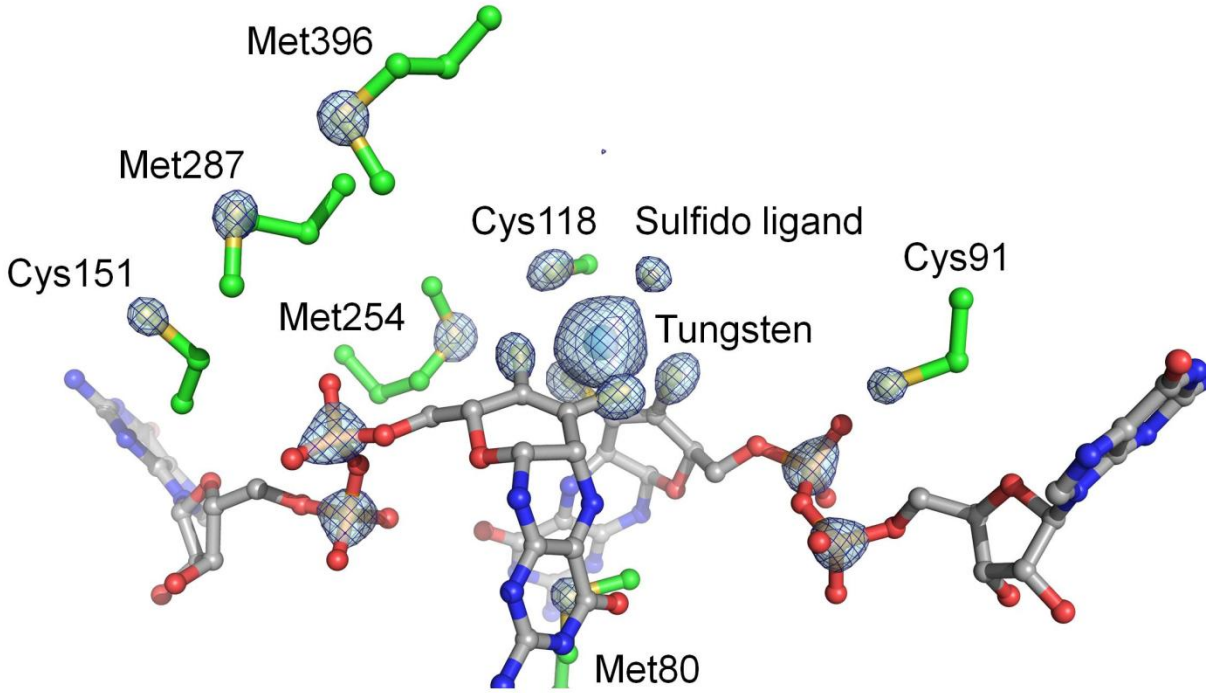

Fig. S5

Sulfide groups coordinated to the tungsten center. The active site of FwdBD with tungstopterin, tungsten, sulfido ligand and the surrounding methionines and cysteines are shown as ball-and-stick models. The $2F_o$-F_c map was contoured at 7σ to highlight that the inorganic tungsten ligand is a sulfur and definitively not an oxygen.

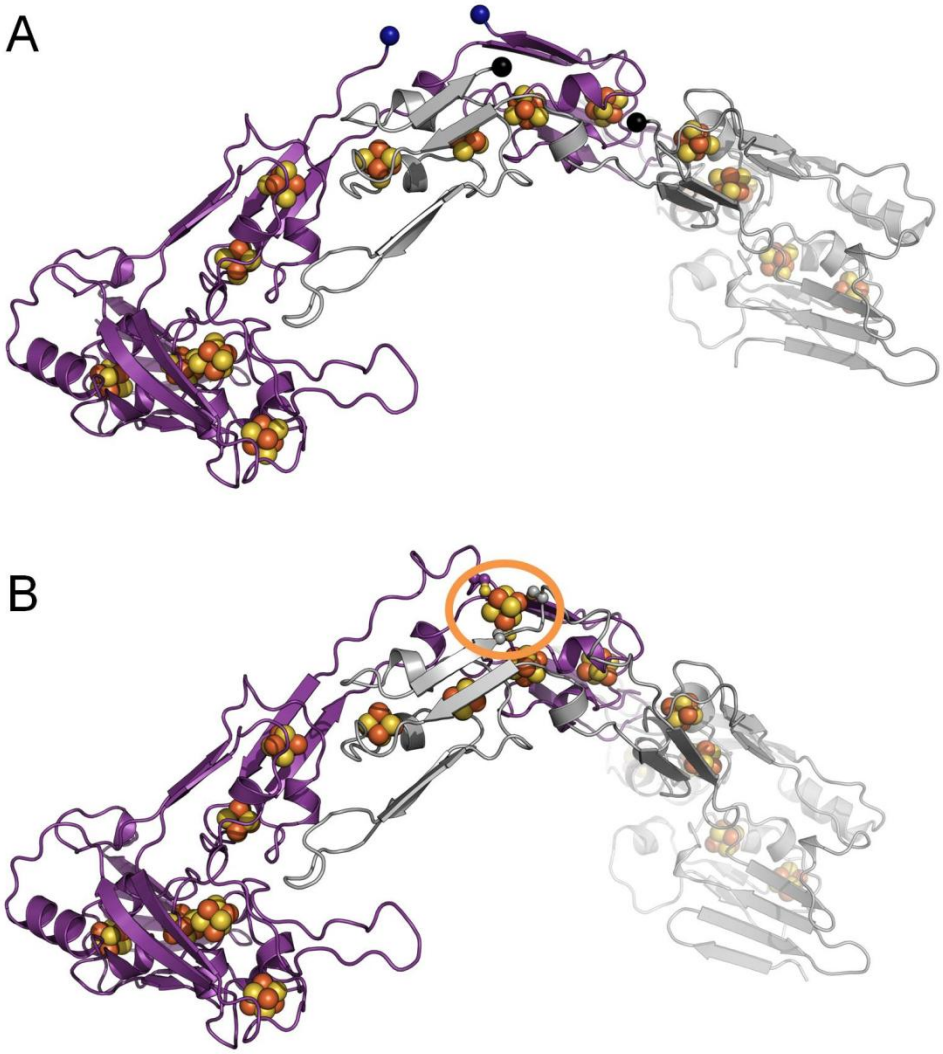

Fig. S6

Localization of an additional [4Fe-4S] cluster in the FwdF dimer. The dimer of two FwdF polyferredoxins (violet and grey) is shown as a cartoon; the [4Fe-4S] clusters are shown as ball models. (**A**) FwdF dimer of the Fwd(ABCDFG)$_2$ dodecamer (12-mer) structure derived from the orthorhombic crystal form. Loops 214–224 are disordered and the terminal residues visible are indicated by blue and black balls. (**B**), FwdF dimer of the Fwd(ABCDFG)$_4$ (24-mer) structure derived from the triclinic crystal form. Loops 214–224 are now ordered and wrapped around an extra [4Fe-4S] cluster, highlighted by an orange circle.

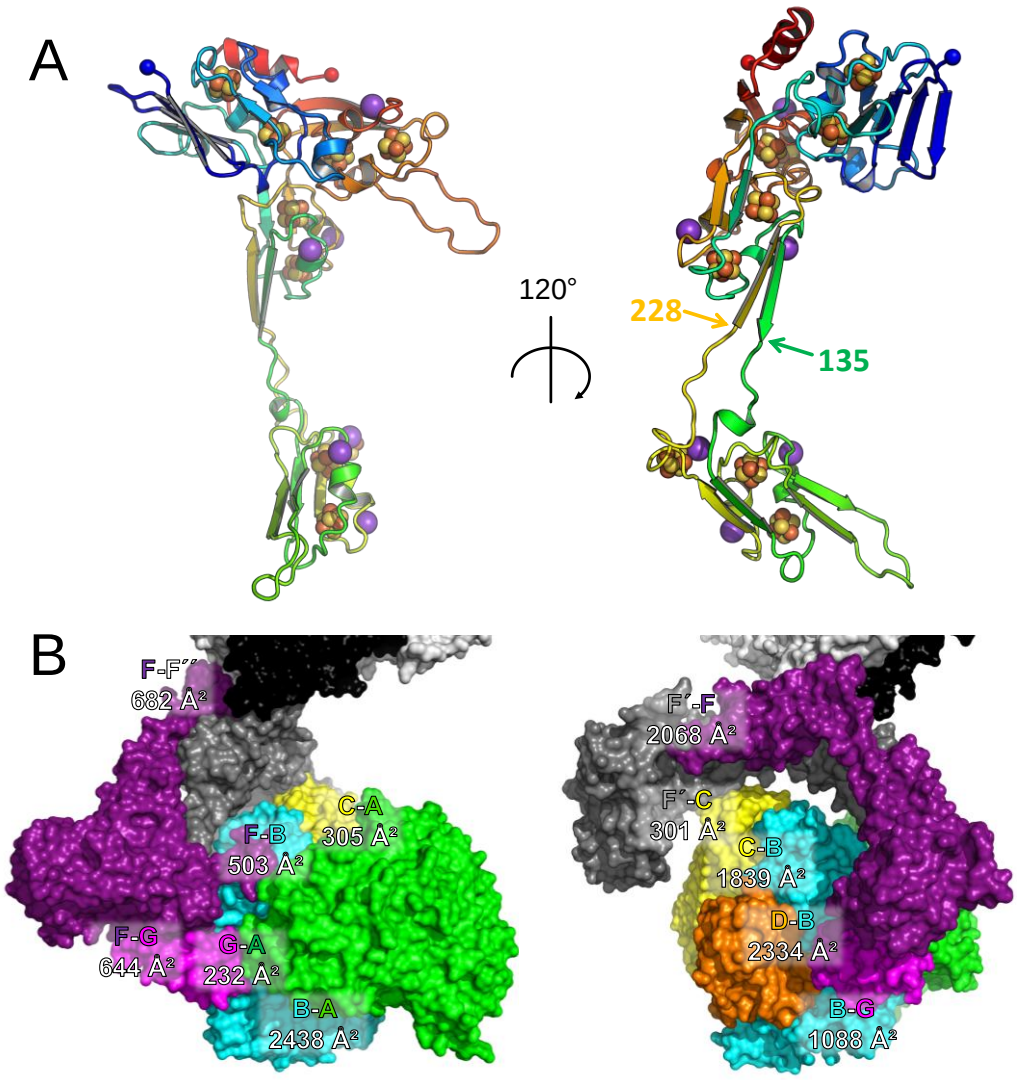

Fig. S7

FwdF organization and interaction mapping. (**A**) Cartoon representation of an FwdF monomer. The polypeptide trace is visualized using a rainbow color code from the N-terminal (blue) to the C-terminal (red) ends; the N-, and C-termini are depicted by a sphere. The second ferredoxin domain is built up with the two separated parts of the FwdF protein (orange and green). Thus, the third ferredoxin (143-221) is inserted into the second ferredoxin (106–137 and 228–257). The position of the amino-acid residue at 135 and 228 are indicated. The [4Fe-4S] clusters and the potassium ions (in violet) bound to the surface loops are shown as balls. FwdF is composed of four ferredoxin modules, each containing two [4Fe-4S] clusters enveloped by two two-stranded antiparallel β-sheets and two α-helices in the canonical manner. (**B**) Interfaces between the Fwd subunits. Each subunit is colored as in Fig. 1. The contact area (in Å) was calculated using the PISA server (*42*).

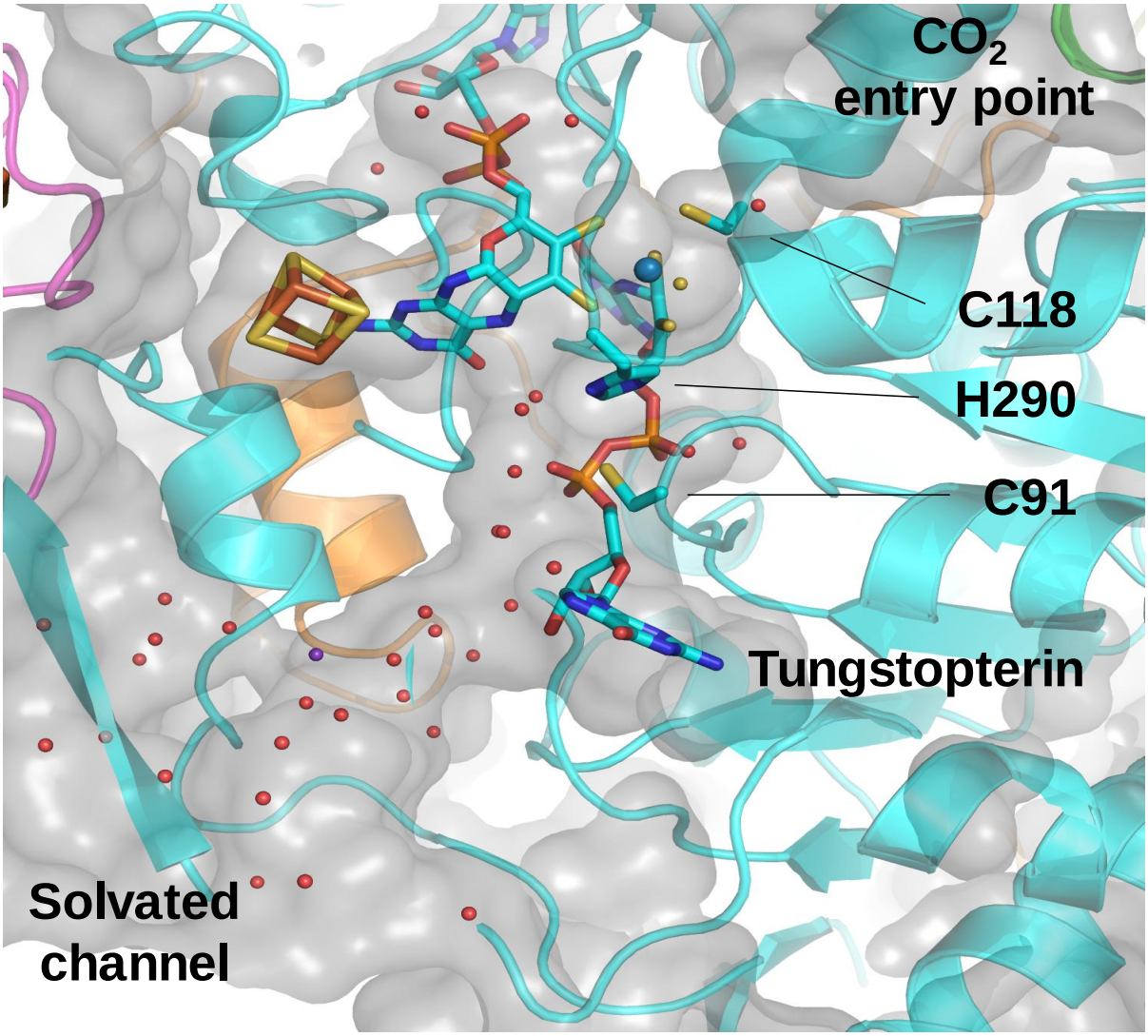

Fig. S8

Hydrophilic cavity (grey surface) in FwdB (blue cartoon) probably responsible for proton-trafficking. The cavity is highly hydrated; the water molecules are shown by red spheres. Amino-acid residues close to tungsten are indicated. Pink and orange cartoons correspond to FwdG and FwdD, respectively.

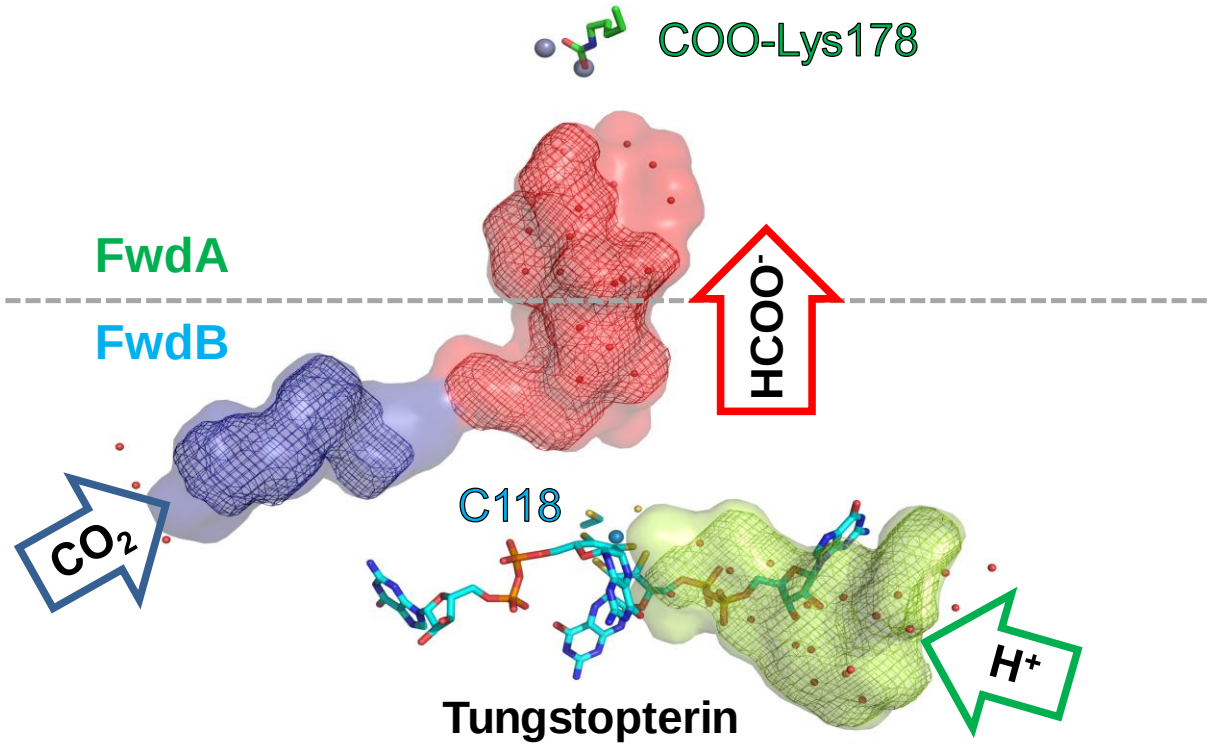

Fig. S9

Overall view of the three putative protein channels in FwdA and FwdB. The hydrophobic CO_2 channel, hydrophilic formate channel and hydrophilic proton channel are indicated by blue, red and green colors. The cavity was calculated using KVfinder (*43*). The surface representation corresponds to a probe of 1 Å and the mesh surface to a probe of 1.4 Å.

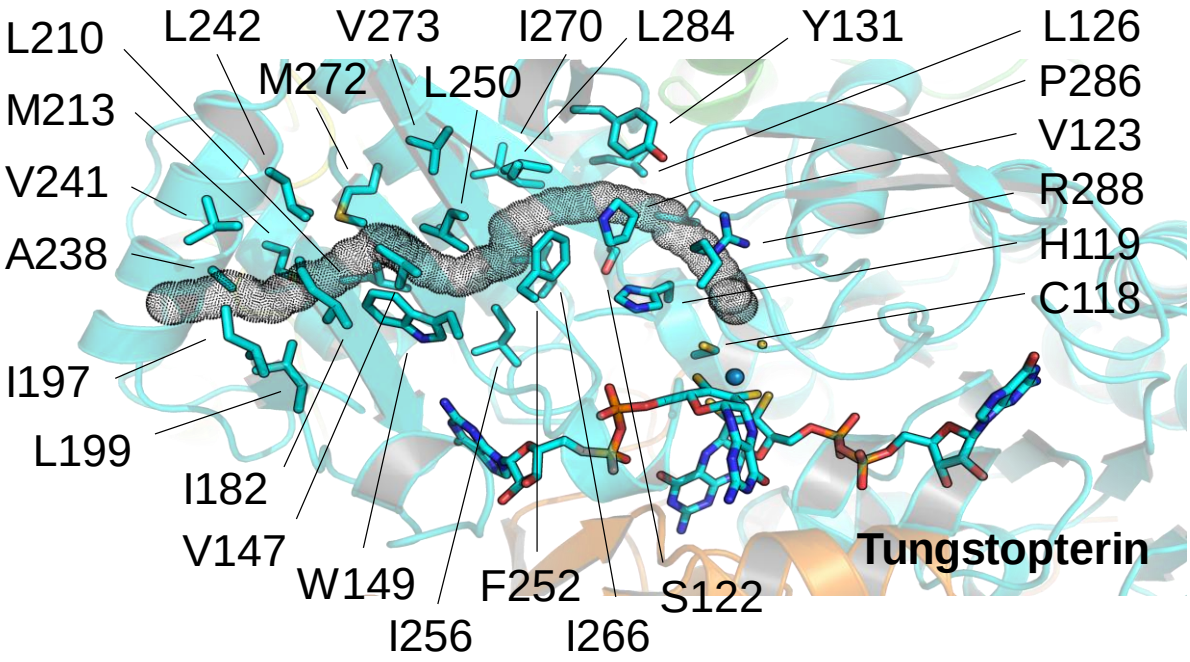

Fig. S10

Hydrophobic cavity of FwdB proposed as a CO_2 channel. The putative CO_2 channel is shown by black mesh. There is no water molecule found in this channel. Amino-acid residues surrounding the cavity are depicted in stick models and labeled.

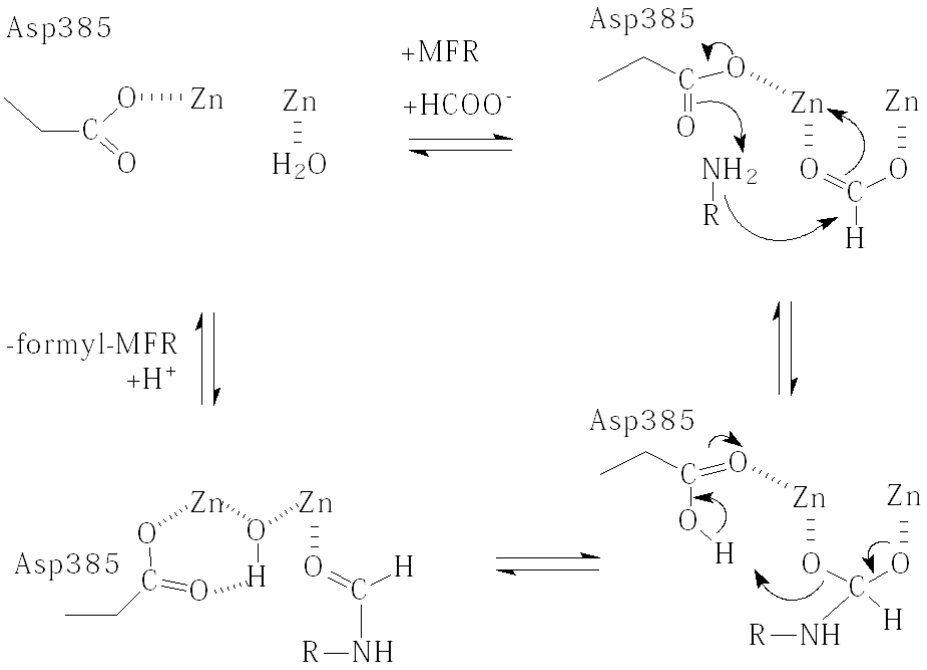

Fig. S11

A catalytic mechanism based on that of dihydroorotase (*14*). R-NH_2 corresponds to the methanofuran (MFR). The nucleophilic attack of the amine group onto formate is facilitated by Asp385 acting as a general base and by two Zn^{2+} which stabilize the negatively charged tetrahedral transition state and make the formate carbon more electrophilic.

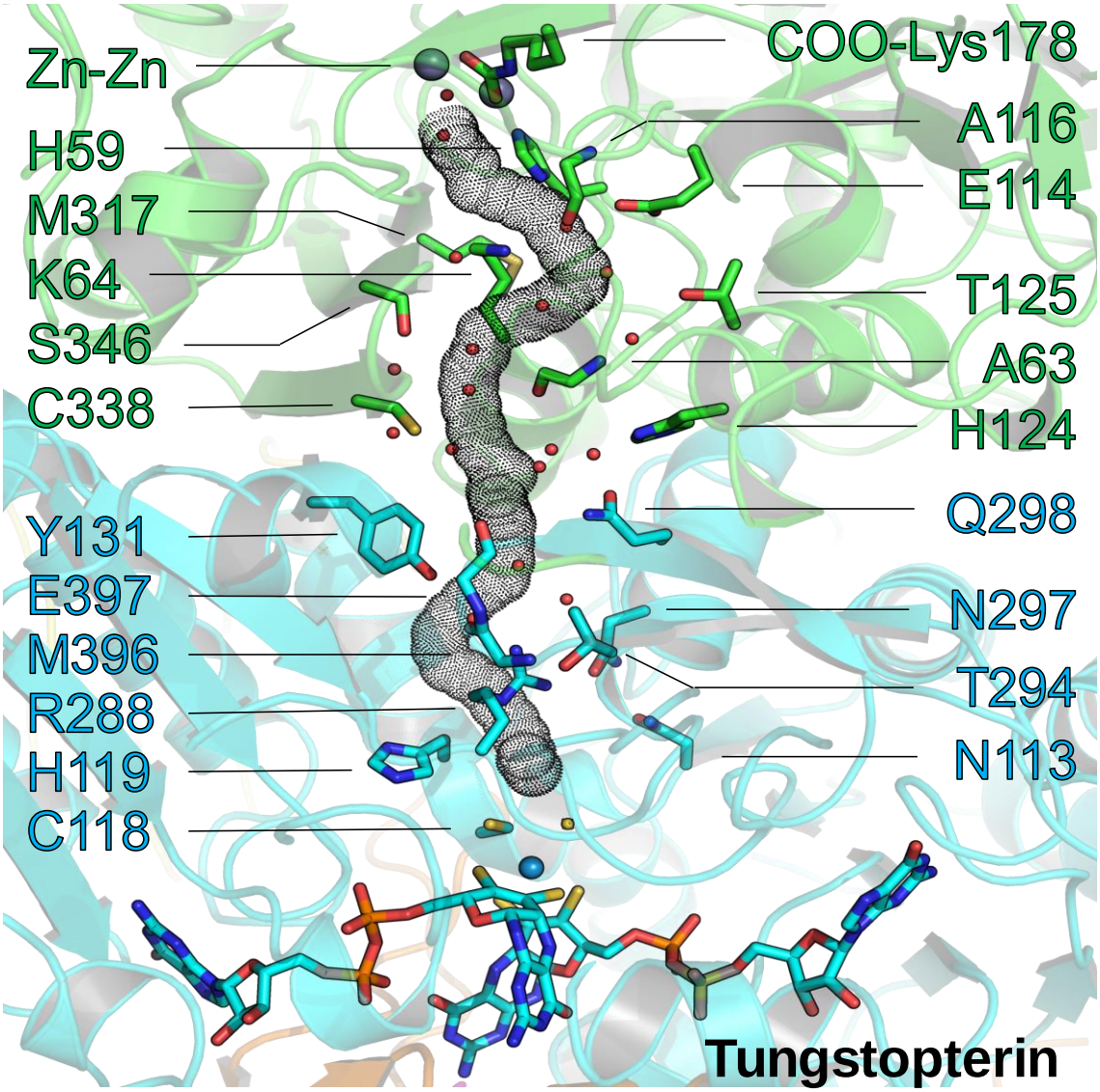

Fig. S12

Hydrophilic cavity between FwdB (cyan) and FwdA (green) proposed as a formate channel. The putative formate channel is shown by black mesh. The cavity is highly hydrated; the water molecules are shown by red spheres. Hydrophilic amino-acid residues making the cavity are depicted in stick models and labeled.

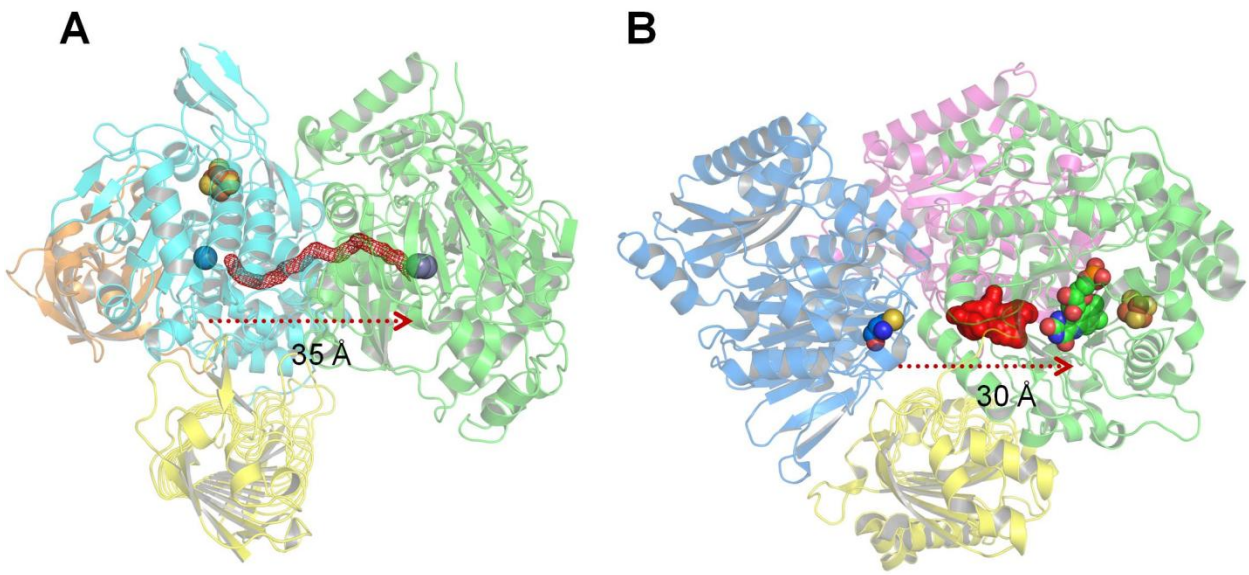

Fig. S13

Comparison of the Fwd complex and glutamate synthase (PDB: 1EA0). (**A**) The catalytic section of the Fwd complex, which is composed of the amidohydrolase FwdA (green) and formate dehydrogenase FwdBD (cyan, orange), is associated with the β-helicoidal FwdC (yellow). The iron-sulfur cluster (orange and yellow spheres) and tungsten (blue sphere) in FwdB, binuclear zinc site (gray spheres) in FwdA, and the formate tunnel (red mesh) are shown. (**B**) Glutamate synthase from *Azospirillum brasilense* (PDB: 1EA0), with Cys1 (carbons in blue), FMN (carbons in green) and an iron-sulfur cluster (orange and yellow) depicted as spheres. The tunnel for ammonia transfer is shown as a red surface. Glutamate synthase and the Fwd complex share a β-helicoidal module (yellow). Both β-helicoidal modules bind to the two catalytic modules and thus might assist in maintaining the tunnel architecture for the transfer of the catalytic intermediate ammonia or formate.

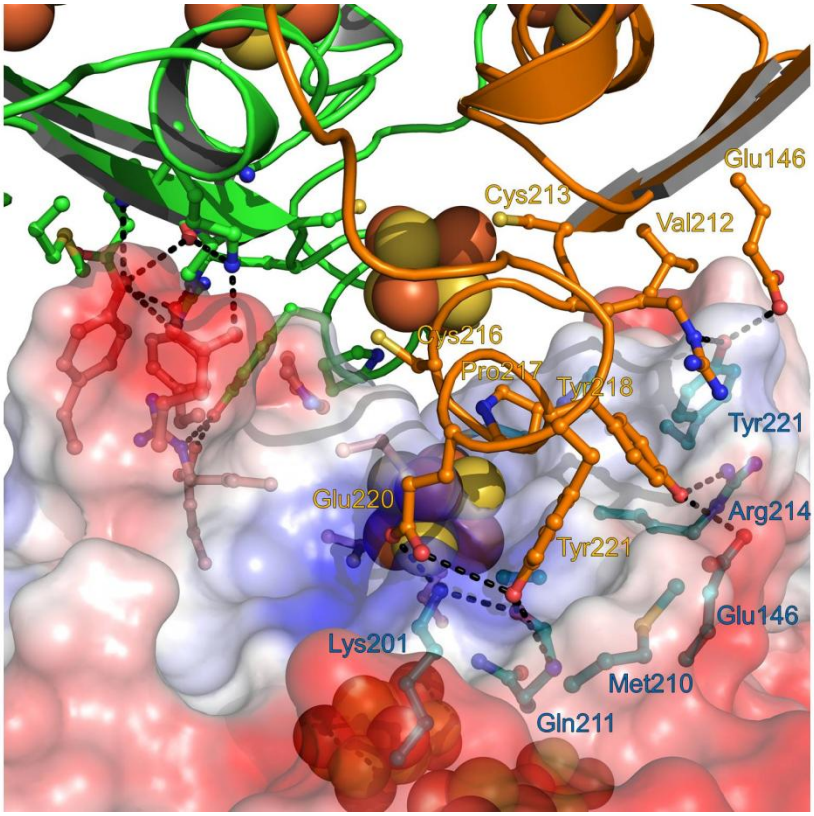

Fig. S14

Interface between the two Fwd(ABCDFG)$_2$ dodecamers (12-mers) in 24-mers. One dimer is shown as a cartoon; the other is represented by an electrostatic surface with negative and positive potentials in red and blue, respectively, which emphasizes the charge clamp interaction. Only one monomer from each symmetrical dimer is labeled. Hydrogen bonds and salt bridges are depicted as black dashed lines.

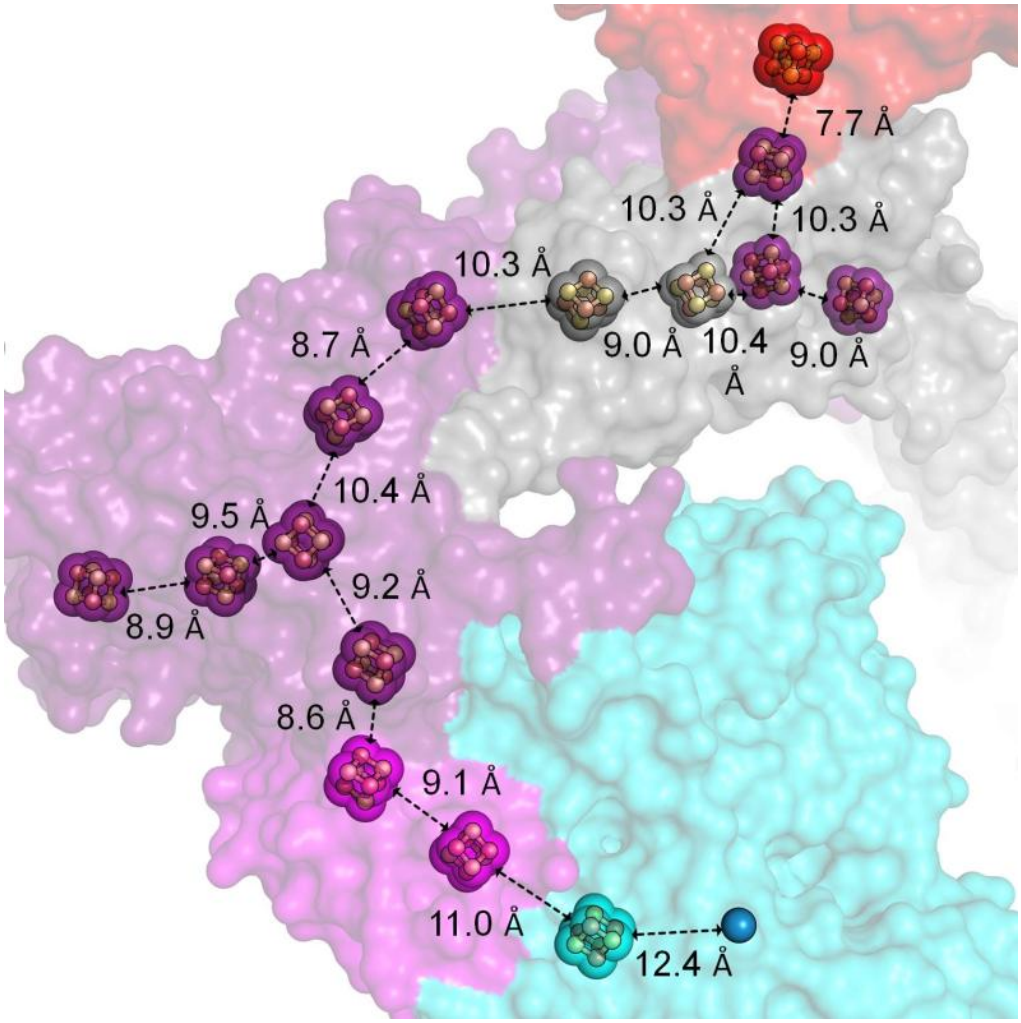

Fig. S15

Electron relay in the Fwd complex. The subunits harboring the [4Fe-4S] clusters are shown as a transparent surface that is color-coded as in Fig. 1 in the main text. The symmetry-related FwdF of Fwd(ABCDFG)$_2$ (12-mer) is drawn in grey, and the extra [4Fe-4S] cluster of FwdF of the second 12-mer is drawn in red. The distances between the closest atoms are labeled. The tungsten center is drawn as a blue ball. All [4Fe-4S] clusters and tungsten are sufficiently close to allow rapid electron transfer.

Table S1 X-ray analysis statistics.

	Fwd(ABCDFG)$_2$ SAD, *P*2$_1$2$_1$2$_1$	**Fwd(ABCDFG)$_4$ bound MFR, *P*1**	**Fwd(ABCDFG)$_2$ *P*3$_2$21**	**Fwd(ABCDFG)$_4$ *P*3$_2$21**
Data collection				
Wavelength (Å)	1.21372	1.00006	1.00005	1.21400
Space group	*P*2$_1$2$_1$2$_1$	*P*1	*P*3$_2$21	*P*3$_2$21
Resolution (Å)	49.26 – 1.90 (2.00 – 1.90)	49.08 – 2.55 (2.69 – 2.55)	48.65 – 2.50 (2.64 – 2.50)	48.75 – 4.20 (4.43 – 4.20)
Cell dimensions				
a, b, c (Å)	121.64, 174.58, 205.43	174.18, 173.68, 183.16	105.54, 105.54, 340.55	288.21, 288.21, 120.30
α, β, γ (°)	90.00, 90.00, 90.00	89.98, 95.42, 92.14	90.00, 90.00, 120.00	90.00, 90.00, 120.00
R_{merge} (%)[a]	9.1 (66.7)	14.0 (69.8)	9.0 (94.0)	15.6 (158.3)
R_{pim} (%)[a]	5.4 (43.7)	10.2 (52.7)	3.5 (35.8)	6.5 (66.3)
$CC_{1/2}$[a]	99.7 (72.6)	97.9 (46.5)	99.8 (79.9)	99.9 (54.7)
I/σ_I[a]	9.2 (1.6)	5.5 (1.5)	13.6 (2.2)	8.4 (1.3)
Completeness (%)[a]	99.2 (96.9)	96.8 (97.0)	100.0 (100.0)	99.9 (100.0)
Redundancy[a]	3.6 (3.1)	2.6 (2.4)	7.5 (7.8)	6.8 (6.7)
Number of unique reflections[a]	339,028 (47,921)	673,754 (98,739)	77,304 (11,126)	42,094 (6,097)
Refinement				
Resolution (Å)	48.49 – 1.90	48.97 – 2.55	48.22 – 2.50	
Number of reflections	338,906	673,055	77,174	
R_{work}/R_{free}[b] (%)	15.32 / 17.21	23.07 / 25.93	15.87 / 18.17	
Number of atoms				
Protein	27,856	111,691	13,947	
Ligands/ions	453	2,017	208	
Solvent	2,506	613	260	
Refined B-values (Å^2)	31	46	68	
Protein/tungstopterin/ [4Fe4S]/ions/H_2O/MFR	31/21/ 26/30/39/-	47/38/ 40/47/39/73	69/59/ 59/71/58/-	
Wilson B-values (Å^2)	25	40	58.3	
Molprobity clash score, all atoms	0.23 (100th percentile)	7.6 (98th percentile)	1.97 (100th percentile)	
Ramachandran plot				
Favoured regions (%)	3,509 (97.3)	13,942 (96.6)	1,743 (96.7)	
Outlier regions (%)	1 (0.03)	26 (0.18)	1 (0.06)	
rmsd[c] bond lengths (Å)	0.010	0.008	0.011	
rmsd[c] bond angles (°)	1.22	1.59	1.67	
PDB code	5T5I	5T61	5T5M	

[a] Values relative to the highest resolution shell are within parentheses. [b] R_{free} was calculated as the R_{work} for 5% of the reflections that were not included in the refinement. [c] rmsd, root mean square deviation.

References and Notes

1. R. K. Thauer, A. K. Kaster, H. Seedorf, W. Buckel, R. Hedderich, Methanogenic archaea: Ecologically relevant differences in energy conservation. *Nat. Rev. Microbiol.* **6**, 579–591 (2008). Medline doi:10.1038/nrmicro1931

2. P. A. Bertram, R. K. Thauer, Thermodynamics of the formylmethanofuran dehydrogenase reaction in *Methanobacterium thermoautotrophicum*. *Eur. J. Biochem.* **226**, 811–818 (1994). Medline doi:10.1111/j.1432-1033.1994.t01-1-00811.x

3. P. A. Bertram, M. Karrasch, R. A. Schmitz, R. Böcher, S. P. Albracht, R. K. Thauer, Formylmethanofuran dehydrogenases from methanogenic Archaea. Substrate specificity, EPR properties and reversible inactivation by cyanide of the molybdenum or tungsten iron-sulfur proteins. *Eur. J. Biochem.* **220**, 477–484 (1994). Medline doi:10.1111/j.1432-1033.1994.tb18646.x

4. R. A. Schmitz, S. P. J. Albracht, R. K. Thauer, A molybdenum and a tungsten isoenzyme of formylmethanofuran dehydrogenase in the thermophilic archaeon *Methanobacterium wolfei*. *Eur. J. Biochem.* **209**, 1013–1018 (1992). Medline doi:10.1111/j.1432-1033.1992.tb17376.x

5. R. A. Schmitz, S. P. J. Albracht, R. K. Thauer, Properties of the tungsten-substituted molybdenum formylmethanofuran dehydrogenase from *Methanobacterium wolfei*. *FEBS Lett.* **309**, 78–81 (1992). Medline doi:10.1016/0014-5793(92)80743-Z

6. R. A. Schmitz, M. Richter, D. Linder, R. K. Thauer, A tungsten-containing active formylmethanofuran dehydrogenase in the thermophilic archaeon *Methanobacterium wolfei*. *Eur. J. Biochem.* **207**, 559–565 (1992). Medline doi:10.1111/j.1432-1033.1992.tb17082.x

7. A. Hochheimer, R. A. Schmitz, R. K. Thauer, R. Hedderich, The tungsten formylmethanofuran dehydrogenase from *Methanobacterium thermoautotrophicum* contains sequence motifs characteristic for enzymes containing molybdopterin dinucleotide. *Eur. J. Biochem.* **234**, 910–920 (1995). Medline doi:10.1111/j.1432-1033.1995.910_a.x

8. A. Hochheimer, R. Hedderich, R. K. Thauer, The formylmethanofuran dehydrogenase isoenzymes in *Methanobacterium wolfei* and *Methanobacterium thermoautotrophicum*: Induction of the molybdenum isoenzyme by molybdate and constitutive synthesis of the tungsten isoenzyme. *Arch. Microbiol.* **170**, 389–393 (1998). Medline doi:10.1007/s002030050658

9. A. Hochheimer, D. Linder, R. K. Thauer, R. Hedderich, The molybdenum formylmethanofuran dehydrogenase operon and the tungsten formylmethanofuran dehydrogenase operon from *Methanobacterium thermoautotrophicum*. Structures and transcriptional regulation. *Eur. J. Biochem.* **242**, 156–162 (1996). Medline doi:10.1111/j.1432-1033.1996.0156r.x

10. S. Bartoschek, J. A. Vorholt, R. K. Thauer, B. H. Geierstanger, C. Griesinger, *N*-carboxymethanofuran (carbamate) formation from methanofuran and CO_2 in methanogenic archaea. Thermodynamics and kinetics of the spontaneous reaction. *Eur. J. Biochem.* **267**, 3130–3138 (2000). Medline doi:10.1046/j.1432-1327.2000.01331.x

11. J. A. Vorholt, R. K. Thauer, The active species of 'CO_2' utilized by formylmethanofuran dehydrogenase from methanogenic Archaea. *Eur. J. Biochem.* **248**, 919–924 (1997). Medline doi:10.1111/j.1432-1033.1997.00919.x

12. L. R. Celeste, G. Chai, M. Bielak, W. Minor, L. L. Lovelace, L. Lebioda, Mechanism of N^{10}-formyltetrahydrofolate synthetase derived from complexes with intermediates and inhibitors. *Protein Sci.* **21**, 219–228 (2012). Medline doi:10.1002/pro.2005

13. Materials and methods are available as supplementary materials on *Science* Online.

14. J. B. Thoden, G. N. Phillips Jr., T. M. Neal, F. M. Raushel, H. M. Holden, Molecular structure of dihydroorotase: A paradigm for catalysis through the use of a binuclear metal center. *Biochemistry* **40**, 6989–6997 (2001). Medline doi:10.1021/bi010682i

15. J. C. Boyington, V. N. Gladyshev, S. V. Khangulov, T. C. Stadtman, P. D. Sun, Crystal structure of formate dehydrogenase H: Catalysis involving Mo, molybdopterin, selenocysteine, and an Fe_4S_4 cluster. *Science* **275**, 1305–1308 (1997). Medline doi:10.1126/science.275.5304.1305

16. H. Raaijmakers, S. Macieira, J. M. Dias, S. Teixeira, S. Bursakov, R. Huber, J. J. G. Moura, I. Moura, M. J. Romão, Gene sequence and the 1.8 Å crystal structure of the tungsten-containing formate dehydrogenase from *Desulfovibrio gigas*. *Structure* **10**, 1261–1272 (2002). Medline doi:10.1016/S0969-2126(02)00826-2

17. L. B. Maia, J. J. G. Moura, I. Moura, Molybdenum and tungsten-dependent formate dehydrogenases. *J. Biol. Inorg. Chem.* **20**, 287–309 (2015). Medline doi:10.1007/s00775-014-1218-2

18. M. Jormakka, S. Törnroth, B. Byrne, S. Iwata, Molecular basis of proton motive force generation: Structure of formate dehydrogenase-N. *Science* **295**, 1863–1868 (2002). Medline doi:10.1126/science.1068186

19. C. Binda, R. T. Bossi, S. Wakatsuki, S. Arzt, A. Coda, B. Curti, M. A. Vanoni, A. Mattevi, Cross-talk and ammonia channeling between active centers in the unexpected domain arrangement of glutamate synthase. *Structure* **8**, 1299–1308 (2000). Medline doi:10.1016/S0969-2126(00)00540-2

20. J. S. Blanchard, W. W. Cleland, Kinetic and chemical mechanisms of yeast formate dehydrogenase. *Biochemistry* **19**, 3543–3550 (1980). Medline doi:10.1021/bi00556a020

21. B. K. Pomper, O. Saurel, A. Milon, J. A. Vorholt, Generation of formate by the formyltransferase/hydrolase complex (Fhc) from *Methylobacterium extorquens* AM1. *FEBS Lett.* **523**, 133–137 (2002). Medline doi:10.1016/S0014-5793(02)02962-9

22. H. Dobbek, V. Svetlitchnyi, L. Gremer, R. Huber, O. Meyer, Crystal structure of a carbon monoxide dehydrogenase reveals a [Ni-4Fe-5S] cluster. *Science* **293**, 1281–1285 (2001). Medline doi:10.1126/science.1061500

23. T. I. Doukov, T. M. Iverson, J. Seravalli, S. W. Ragsdale, C. L. Drennan, A Ni-Fe-Cu center in a bifunctional carbon monoxide dehydrogenase/acetyl-CoA synthase. *Science* **298**, 567–572 (2002). Medline doi:10.1126/science.1075843

24. X. Huang, H. M. Holden, F. M. Raushel, Channeling of substrates and intermediates in enzyme-catalyzed reactions. *Annu. Rev. Biochem.* **70**, 149–180 (2001). Medline doi:10.1146/annurev.biochem.70.1.149

25. K. C. Costa, P. M. Wong, T. Wang, T. J. Lie, J. A. Dodsworth, I. Swanson, J. A. Burn, M. Hackett, J. A. Leigh, Protein complexing in a methanogen suggests electron bifurcation and electron delivery from formate to heterodisulfide reductase. *Proc. Natl. Acad. Sci. U.S.A.* **107**, 11050–11055 (2010). Medline doi:10.1073/pnas.1003653107

26. K. C. Costa, T. J. Lie, Q. Xia, J. A. Leigh, VhuD facilitates electron flow from H_2 or formate to heterodisulfide reductase in *Methanococcus maripaludis*. *J. Bacteriol.* **195**, 5160–5165 (2013). Medline doi:10.1128/JB.00895-13

27. A. Volbeda, M. H. Charon, C. Piras, E. C. Hatchikian, M. Frey, J. C. Fontecilla-Camps, Crystal structure of the nickel-iron hydrogenase from *Desulfovibrio gigas*. *Nature* **373**, 580–587 (1995). Medline doi:10.1038/373580a0

28. J. W. Peters, W. N. Lanzilotta, B. J. Lemon, L. C. Seefeldt, X-ray crystal structure of the Fe-only hydrogenase (CpI) from *Clostridium pasteurianum* to 1.8 angstrom resolution. *Science* **282**, 1853–1858 (1998). Medline doi:10.1126/science.282.5395.1853

29. S. Santabarbara, P. Heathcote, M. C. W. Evans, Modelling of the electron transfer reactions in Photosystem I by electron tunnelling theory: The phylloquinones bound to the PsaA and the PsaB reaction centre subunits of PS I are almost isoenergetic to the iron-sulfur cluster F_X. *Biochim. Biophys. Acta* **1708**, 283–310 (2005). Medline doi:10.1016/j.bbabio.2005.05.001

30. A. Esteve-Núñez, J. Sosnik, P. Visconti, D. R. Lovley, Fluorescent properties of c-type cytochromes reveal their potential role as an extracytoplasmic electron sink in *Geobacter sulfurreducens*. *Environ. Microbiol.* **10**, 497–505 (2008). Medline doi:10.1111/j.1462-2920.2007.01470.x

31. K. D. Bewley, K. E. Ellis, M. A. Firer-Sherwood, S. J. Elliott, Multi-heme proteins: Nature's electronic multi-purpose tool. *Biochim. Biophys. Acta* **1827**, 938–948 (2013). Medline doi:10.1016/j.bbabio.2013.03.010

32. J. N. Reeve, G. S. Beckler, D. S. Cram, P. T. Hamilton, J. W. Brown, J. A. Krzycki, A. F. Kolodziej, L. Alex, W. H. Orme-Johnson, C. T. Walsh, A hydrogenase-linked gene in *Methanobacterium thermoautotrophicum* strain ΔH encodes a polyferredoxin. *Proc. Natl. Acad. Sci. U.S.A.* **86**, 3031–3035 (1989). Medline doi:10.1073/pnas.86.9.3031

33. W. Kabsch, Xds. *Acta Crystallogr. D* **66**, 125–132 (2010). Medline doi:10.1107/S0907444909047337

34. M. D. Winn, C. C. Ballard, K. D. Cowtan, E. J. Dodson, P. Emsley, P. R. Evans, R. M. Keegan, E. B. Krissinel, A. G. W. Leslie, A. McCoy, S. J. McNicholas, G. N. Murshudov, N. S. Pannu, E. A. Potterton, H. R. Powell, R. J. Read, A. Vagin, K. S. Wilson, Overview of the CCP4 suite and current developments. *Acta Crystallogr. D* **67**, 235–242 (2011). Medline doi:10.1107/S0907444910045749

35. G. M. Sheldrick, A short history of SHELX. *Acta Crystallogr. A* **64**, 112–122 (2008). Medline doi:10.1107/S0108767307043930

36. G. Langer, S. X. Cohen, V. S. Lamzin, A. Perrakis, Automated macromolecular model building for X-ray crystallography using ARP/wARP version 7. *Nat. Protoc.* **3**, 1171–1179 (2008). Medline doi:10.1038/nprot.2008.91

37. A. Vagin, A. Teplyakov, *MOLREP*: An automated program for molecular replacement. *J. Appl. Cryst.* **30**, 1022–1025 (1997). doi:10.1107/S0021889897006766

38. P. V. Afonine, R. W. Grosse-Kunstleve, V. B. Chen, J. J. Headd, N. W. Moriarty, J. S. Richardson, D. C. Richardson, A. Urzhumtsev, P. H. Zwart, P. D. Adams, *phenix.model_vs_data*: A high-level tool for the calculation of crystallographic model and data statistics. *J. Appl. Crystallogr.* **43**, 669–676 (2010). Medline doi:10.1107/S0021889810015608

39. P. Emsley, K. Cowtan, Coot: Model-building tools for molecular graphics. *Acta Crystallogr. D* **60**, 2126–2132 (2004). Medline doi:10.1107/S0907444904019158

40. G. N. Murshudov, A. A. Vagin, E. J. Dodson, Refinement of macromolecular structures by the maximum-likelihood method. *Acta Crystallogr. D* **53**, 240–255 (1997). Medline doi:10.1107/S0907444996012255

41. E. Chovancova, A. Pavelka, P. Benes, O. Strnad, J. Brezovsky, B. Kozlikova, A. Gora, V. Sustr, M. Klvana, P. Medek, L. Biedermannova, J. Sochor, J. Damborsky, CAVER 3.0: A tool for the analysis of transport pathways in dynamic protein structures. *PLOS Comput. Biol.* **8**, e1002708 (2012). Medline doi:10.1371/journal.pcbi.1002708

42. E. Krissinel, K. Henrick, Inference of macromolecular assemblies from crystalline state. *J. Mol. Biol.* **372**, 774–797 (2007). Medline doi:10.1016/j.jmb.2007.05.022

43. S. H. P. Oliveira, F. A. N. Feraz, R. V. Honorato, J. Xavier-Neto, T. J. P. Sobreira, P. S. de Oliveira, KVFinder: Steered identification of protein cavities as a PyMOL plugin. *BMC Bioinformatics* **15**, 197 (2014). Medline doi:10.1186/1471-2105-15-197